Stability Analysis of the Optical Reference Gyro Discrete Noise Eliminator

by

Fredrick S. Gruman

B.S., Electrical Engineering
Texas A&M University (1988)

Submitted to the
Department of Electrical Engineering and Computer Science
in partial fulfillment of the requirements
for the degree of Master of Science
at the
Massachusetts Institute of Technology

May 1994

Signature of Author: _____
Department of Electrical Engineering and Computer Science

Approved by: _____
Michael F. Luniewicz
Member Technical Staff
The Charles Stark Draper Laboratory

Certified by: _____
James K. Roberge
Professor
Department of Electrical Engineering and Computer Science

Accepted by: _____
Frederic R. Morgenthaler
Chairman, Departmental Committee on Graduate Studies

Stability Analysis of the Optical Reference Gyro Discrete Noise Eliminator

by
Fredrick S. Gruman

Submitted to the
Department of Electrical Engineering and Computer Science
in partial fulfillment of the requirements
for the degree of Master of Science
at the
Massachusetts Institute of Technology

May 1994

Abstract

The Charles Stark Draper Laboratory, Inc. developed a pointing stabilization testbed which utilizes an optical reference provided by the spinning rotor of a gyroscope. This gyroscope, however, introduces a discrete noise component into the reference beam at its 90 Hz rotor spin frequency. In previous work, the discrete noise was removed from the reference beam with the discrete noise eliminator, a notch-like device which operates on phase-lock loop principles. But the eliminator causes the stabilization loop to become unstable if the open-loop bandwidth exceeds 60 Hz, and the 60 Hz stabilization loop has an effective jitter stabilization bandwidth (EJSB) of only 35 Hz, where the EJSB is the frequency band with at least 20 dB disturbance rejection. This thesis investigates techniques for extending the EJSB.

A linear model for the eliminator was derived which showed that the eliminator introduces 180° of phase lag at the gyro spin frequency. By adding lead compensation to the stabilization loop, a 240 Hz open-loop bandwidth was demonstrated. But this required a large amount of phase lead resulting in a 20 db reduction in low-frequency disturbance rejection and a decrease in the EJSB to 5 Hz even though the open-loop bandwidth was increased.

A second-order, electronically tunable notch filter was investigated as a replacement for the eliminator. This notch is able to search for and lock onto the discrete noise. Compared to the eliminator, the notch filter introduces only 90° of phase lag at the gyro spin frequency making it easier to extend the bandwidth of the stabilization loop. Using the notch filter, a 212 Hz open-loop bandwidth was demonstrated with an EJSB of 55 Hz without sacrificing low-frequency disturbance rejection.

An improved gyroscope is under development which will increase the spin frequency to 200 Hz. The projected EJBW with this gyroscope is 110 Hz.

Technical Supervisor: Michael F. Luniewicz
Member Technical Staff
The Charles Stark Draper Laboratory, Inc.

Thesis Supervisor: James K. Roberge
Professor
Massachusetts Institute of Technology

Acknowledgment

I would first like to extend my gratitude to my parents, who supported me always.

I would like to express my most sincere thanks to Mike Luniewicz who provided me with invaluable technical direction and guidance. His availability and constant encouragement, along with his thorough knowledge of control systems and hardware implementation, aided tremendously in overcoming the difficulties of this thesis research.I am thankful for the practical help provided by Dale Woodbury. His hands-on experience taught me that there is more to engineering than the theory taught in textbooks. I would like to also thank Professor Roberge for his support and advise; it was he who suggested I investigate the notch filter.

I am indebted to William Sartonowicz for his support in the construction of the hardware components. Without his help, I do not believe I could have finished this thesis on time. I would also like to thank Dr. T. T. Chien who started me on this thesis.

And finally, I would like to thank the United States Air Force and The Charles Stark Draper Laboratory for affording me this opportunity to pursue my graduate studies.

This thesis was prepared at The Charles Stark Draper Laboratory, Inc., under Independent Research and Development Project Number 432.

Table of Contents

List of Figures

Chapter 1: Introduction

1.1 Background

The optical reference gyro, or ORG, is an inertial instrument invented at The Charles Stark Draper Laboratory, Inc. for use as a pointing stabilization reference. Applications of a pointing stabilization reference include high-resolution imaging telescopes and intersatellite optical communications. These are examples where the direction of line-of-sight (LOS) must be precisely maintained even though angular jitter may be present on the support structure of the telescope or the optical receiver. Jitter that couples into the LOS will smear the image of a high-resolution telescope or degrade the signal to noise ratio of an optical communication link.

Some common examples of jitter sources are the pointing drive mechanism, power systems, cryocoolers of infrared sensors, attitude control and solar array drives in satellite systems, vehicle vibration in aircraft systems and seismic motion in ground-based systems. The goal of the ORG stabilization system is to correct for jitter up to a frequency of 100 Hz. Certainly jitter spectra may exceed 100 Hz, but jitter typically rolls off with increasing frequency. Therefore, if significant jitter is present above 100 Hz, it is most often due to the excitation of a mechanical flexing mode rather than due to rigid body motion. When flexing proves to be an unacceptable jitter error source

of a pointing system, then additional stabilization techniques, such as adaptive wavefront control, become necessary.

Typically it is not practical to completely isolate the optical payload from jitter disturbances due to the payload's size and inertia and the proximity of jitter sources. However, although the entire payload is not stabilized, its effective LOS can be stabilized by actively steering a mirror in the optical train to cancel the effect of rigid body motion. A key function needed to control the steering mirror is a wideband reference that indicates the effective LOS pointing error so a mirror control servo can be closed. The ORG serves this function by emitting an inertially stabilized, collimated optical beam. The ORG beam is injected into the optical system, and because the ORG beam is stabilized, the position of its image at the output of the optical system is a direct measure of LOS jitter.

The ORG is a two-degree-of-freedom dry-tuned gyroscope (DTG) that has a collimated light source built into its spinning rotor. Because the rotor of a DTG is inherently inertially stabilized, the beam generated by the rotor-mounted light source is also stabilized - with one exception. Mechanical machining and alignment tolerances limit the alignment accuracy between the rotor's spin axis and its light source axis. As a result the ORG beam cones at the rotor's discrete spin frequency, 90 Hz, and the coning of 11 μrad r.m.s is a large error source. Uncorrected the coning error would make the ORG unusable for many pointing stabilization applications. Therefore Doerr [4] invented a means of correcting the coning error which he called the subtraction mode discrete noise eliminator. Doerr achieved 60 dB of coning attenuation.

Feldgoise [5] installed the ORG, equipped with Doerr's discrete noise eliminator, in a pointing stabilization testbed and evaluated pointing stabilization performance. He found that pointing performance increased in a predictable manner as he increased the bandwidth of his steering mirror control loop. However, he also found that the discrete noise eliminator limited the maximum stable bandwidth of the mirror loop to a unity gain crossover of only 60 Hz which corresponds to an effective jitter stabilization bandwidth[1] of only 35 Hz, far short of the 100 Hz goal.

This bandwidth limitation has been taken into account in the design of an improved ORG which will have a 200 Hz spin speed. Increasing the spin speed to 200 Hz from 90 Hz will increase

1. The *effective jitter stabilization bandwidth* defines the frequency range for which the system isolation, i.e. the transfer function from jitter disturbance to effective LOS, is better than -20 dB.

the effective jitter stabilization bandwidth to about 80 Hz, still shy of the 100 Hz goal. Unfortunately physical constraints on the gyro mechanism limit further increase of the spin speed. Therefore another method of increasing the effective jitter stabilization bandwidth of the ORG-based pointing reference is sought.

1.2 Problem Statement

Because platform jitter is typically a wideband noise process, with significant energy out to 100 Hz, it is desirable to maximize jitter stabilization bandwidth. In Feldgoise's tests, jitter stabilization was effective only to approximately 35 Hz due to a 60 Hz crossover frequency limit imposed on the mirror loop. Interaction of the discrete noise eliminator's dynamics with the mirror loop drove the coupled system unstable for higher frequency loops. Feldgoise's mirror loop design ignored the eliminator.

Two methods for increasing the mirror loop crossover frequency while still achieving the discrete noise eliminator's function have been investigated and documented in this thesis. The first method was to design a new mirror loop controller that takes into account the dynamics of the discrete noise eliminator. To this end a linear time-invariant (LTI) model of the eliminator was derived from the nonlinear eliminator dynamics, and several controllers were designed achieving, theoretically, mirror loop crossover frequencies over 200 Hz. However, the usefulness of these controllers was limited due to either complexity of implementation or because the resulting loop shape, while having reached high frequency crossover, suffered from low open-loop gain above 30 Hz. High open-loop gain is needed to effectively attenuate jitter. One of these controllers was built and tested; the predicted and measured results matched closely.

The second method for increasing the crossover of the mirror loop was to replace the discrete noise eliminator with a notch filter. However, in order to attenuate the discrete noise sufficiently even as the parameters of the notch filter drifted, a tracking notch was designed. The tracking notch filter design resulted in a mirror control loop with a 200 Hz crossover frequency, with loop gain and an effective stabilization bandwidth of 50 Hz using the 90 Hz ORG. This scales to a stabilization bandwidth of 110 Hz for the 200 Hz ORG design. The tracking notch filter was also built and tested.

1.3 Organization

This thesis is organized into six chapters. Chapter 2 describes the mirror loop and models the components that make up this loop. Chapter 3 presents the controller analysis and design for the subtraction eliminator. Chapter 4 details the analysis and controller design for the case when the eliminator is replaced with a linear notch filter. This chapter also details the design of an agile frequency controller that allows the notch filter to lock to and track the 90 Hz discrete disturbance. Chapter 5 describes the hardware implementation of the eliminator and the notch controllers. A summary of test results and a comparison of the eliminator and the notch are also given. Finally, Chapter 6 summarizes the results of this thesis and provides recommendations for future research.

Chapter 2: System Components

The analysis of this thesis deals exclusively with the mirror loop of the pointing stabilization testbed developed by Feldgoise and the interaction of the mirror loop with the pointing of the system to the target beam. For a complete discussion of the pointing stabilization testbed, see [5]. This chapter describes the mirror loop and models the components of the loop.

2.1 The Mirror Loop

The goal of the pointing stabilization testbed is to point at an external target beam and to precisely maintain the LOS in the presence of a disturbance environment. The target beam reflects off the fast steering mirror and is then detected by a receiver. Figure 2-1 shows the block diagram of the target pointing process. In this diagram, θ_{TI} is the external target beam, θ_{MI} is the mirror angle, and θ_{BI} is the base (testbed) motion, where all quantities are angles measured with respect to inertial space. The output of the receiver is denoted e_4 and is a voltage proportional to a sum of the input angles. Since the receiver is fixed to the testbed, any base motion, θ_{BI}, adds negatively to e_4. Movement by the fast-steering mirror is taken into account by adding twice the inertial mirror

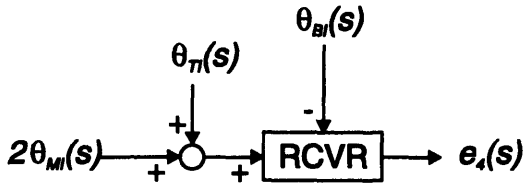

Figure 2-1: Target Pointing Process

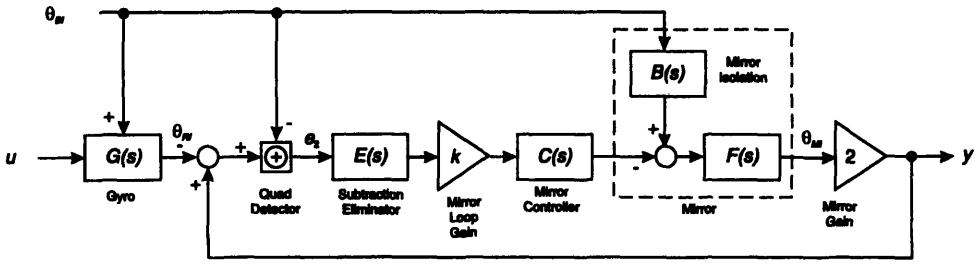

Figure 2-2: Mirror Loop Block Diagram

displacement, θ_{MI}, directly to e_4.[1] The target pointing process is summarized by

$$e_4(s) = \theta_{TI}(s) - \theta_{BI}(s) + 2\theta_{MI}(s) \qquad (2\text{-}1)$$

The mirror is driven by a servo loop in an effort to cancel any base motion disturbance from the target pointing process. The mirror loop block diagram, as implemented by Feldgoise, is shown in Figure 2-2. The optical reference, θ_{RI}, is produced by the ORG. This signal is observed by the quad detector after it is reflected off the fast-steering mirror. Since the quad detector is fixed

1. The factor of two represents the *mirror gain*. Let a signal be reflected off a mirror and let the mirror rotate by an angle θ. Then the reflected signal will undergo a rotation of 2θ.

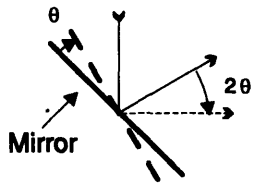

to the testbed, it also observes base motion, θ_{BI}. If the quad output is denoted e_2, then the quad detection process is modeled by

$$e_2(s) = -\theta_{RI}(s) - \theta_{BI}(s) + 2\theta_{MI}(s) \tag{2-2}$$

The signal e_2 is the input to the mirror controller which in turn drives the mirror. The mirror is modeled as two transfer functions: $F(s)$ describes how the controller output affects the mirror output, θ_{MI}, recalling that θ_{MI} is the mirror angle measured with respect to inertial coordinates, and $B(s)$ is the mirror isolation such that $F(s)B(s)$ describes how base motion, θ_{BI}, couples to θ_{MI}. Through closed-loop feedback, the mirror loop tends to drive e_2 to zero (within the bandwidth of the mirror loop). If it is assumed that the optical reference is perfect, i.e., $\theta_{RI} = 0$, then the mirror will be driven so that $\theta_{MI}(s) \cong \frac{1}{2}\theta_{BI}(s)$. Thus by nulling the reference beam on the quad detector, the mirror loop simultaneously cancels the base motion disturbance from e_4 resulting in $e_4(s) \cong \theta_{TI}(s)$.

The optical reference, θ_{RI}, is produced by the spinning rotor of the ORG. With the eliminator in subtraction mode, the torquing inputs to the ORG are zero, i.e. $u = 0$. Let the ORG be replaced with an ideal reference source ($\theta_{RI} = 0$) plus three terms representing imperfections of the gyro: $H(s)\theta_{BI}(s)$, d(s) and n(s). $H(s)$ represents the ORG isolation which characterizes the transfer function between the base motion disturbance θ_{BI} and the reference source θ_{RI}; best performance is achieved with $|H(s)|$ small. The term $d(s)$ represents the primary (largest) noise component of the ORG which is the discrete disturbance at the ORG's spin speed. The term $n(s)$ represents the remainder of the ORG noise. The modified ORG model is then given by

$$\theta_{RI}(s) = H(s)\,\theta_{BI}(s) + d(s) + n(s) \tag{2-3}$$

From Figure 2-2 and Equation (2-3), the transfer function of the mirror loop can be shown to be

$$\theta_{MI}(s) = \frac{F(s)\,[B(s) + kC(s)E(s)\,(1 + H(s))]}{1 + 2kF(s)C(s)E(s)}\theta_{BI}(s) + \frac{kF(s)C(s)E(s)}{1 + 2kF(s)C(s)E(s)}(d(s) + n(s)) \tag{2-4}$$

Combining (2-1) and (2-4) gives the transfer function of the target pointing process:

$$e_4(s) = \theta_{TI}(s) + \frac{2F(s)B(s) - 1 + 2kF(s)C(s)E(s)H(s)}{1 + 2kF(s)C(s)E(s)}\theta_{BI}(s) + \frac{2kF(s)C(s)E(s)}{1 + 2kF(s)C(s)E(s)}(d(s) + n(s)) \tag{2-5}$$

Let both the ORG and mirror perfectly reject any base motion coupling, i.e. assume that the isolations of these components are perfect. For the ORG, this is stated by

$$H(s) = 0 \tag{2-6}$$

and similarly, for the mirror,

$$B(s) = 0 \tag{2-7}$$

Also, assume that the ORG noise term $n(s)$ is zero:

$$n(s) = 0 \tag{2-8}$$

Given these assumptions, (2-5) becomes

$$\begin{aligned} e_4(s) &= \theta_{TI}(s) - \frac{1}{1 + 2kF(s)C(s)E(s)}\theta_{BI}(s) + \frac{2kF(s)C(s)E(s)}{1 + 2kF(s)C(s)E(s)}d(s) \\ &= \theta_{TI}(s) - K_1(s)\theta_{BI}(s) + K_2(s)d(s) \end{aligned} \tag{2-9}$$

Notice that $\theta_{BI}(s)$ and $d(s)$ affect $e_4(s)$ in a complementary manner - the transfer functions from $\theta_{BI}(s)$ to $e_4(s)$ and from $d(s)$ to $e_4(s)$ must add to one: $K_1(s) + K_2(s) = 1$ for all s. If $\theta_{BI}(s)$ is almost completely attenuated from $e_4(s)$ at a given frequency $s = j\omega$, then at the same frequency, $d(s)$ is almost completely transferred to $e_4(s)$, and vice versa. Thus, the effects of $\theta_{BI}(s)$ and $d(s)$ cannot be simultaneously minimized at a given frequency. The components of the mirror loop, specifically the eliminator and the mirror controller, are designed to minimize the effects of $\theta_{BI}(s)$ and $d(s)$ on $e_4(s)$. The transfer function $C(s)$ is designed to minimize $K_1(s)$ in the region where $\theta_{BI}(s)$ is significant, i.e. in the low-frequency region. The transfer function $E(s)$ is designed to minimize $K_2(s)$ in the region where $d(s)$ is significant. Since $d(s)$ is significant only at 90 Hz, $E(s)$ is designed to be a "notch" at that frequency.

An equivalent representation of (2-9) is shown in Figure 2-3.

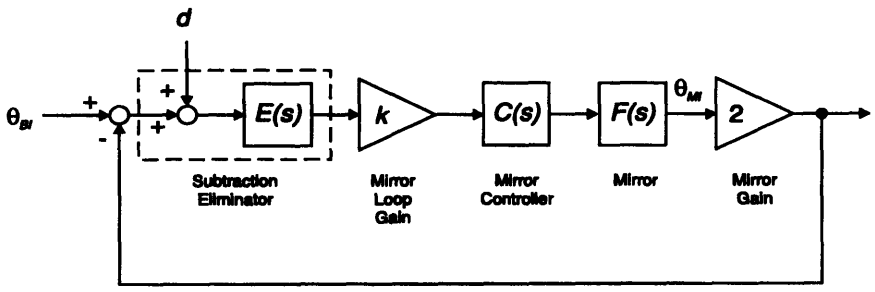

Figure 2-3: Equivalent Mirror Loop Block Diagram

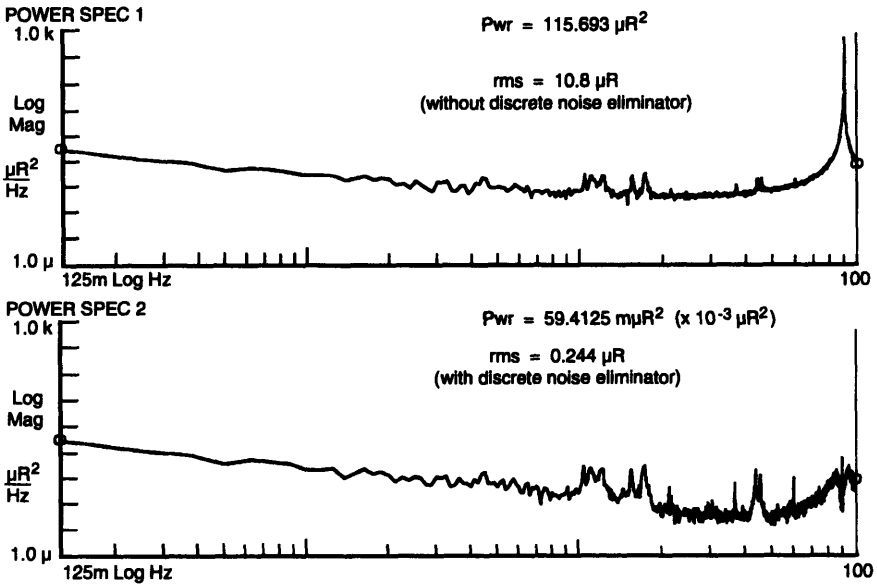

Figure 2-4: Noise Characteristic of the Optical Reference Gyro with and without the Eliminator

2.2 The Subtraction Eliminator

The eliminator was developed by Doerr [4] to reduce the effects of the ORG discrete disturbance, *d(t)*, on system performance. Figure 2-4 [5, page 28] shows the power spectrum of the ORG's noise, i.e. θ_{RI}. From this spectrum, it is seen that the discrete disturbance at 90 Hz is the primary contributor. Figure 2-4 also shows the noise spectrum of the ORG's noise after the eliminator is

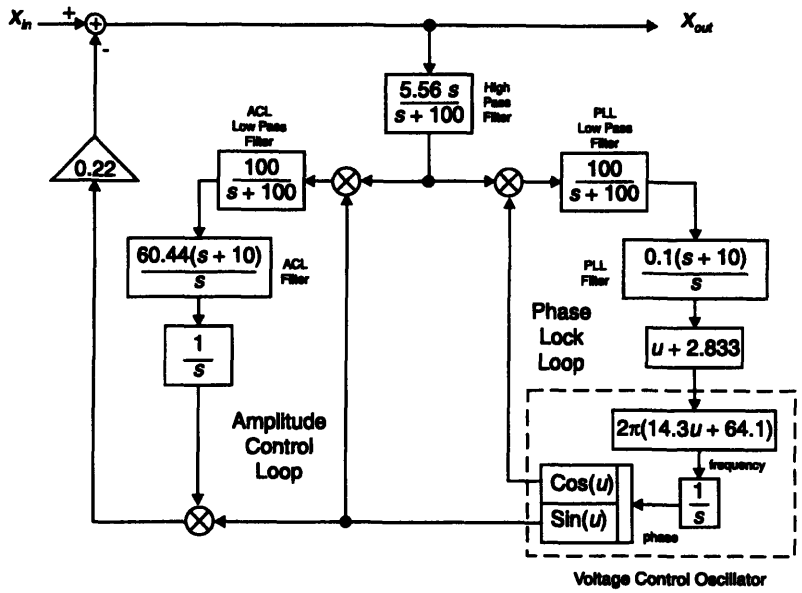

Figure 2-5: Subtraction Eliminator Block Diagram

used to cancel the discrete disturbance. Without the eliminator, the cumulative noise on θ_{RI} over the frequency band of 0.125 Hz to 100 Hz is 10.8 μrad r.m.s. The eliminator reduces the noise over the same band to 0.244 μrad r.m.s. by removing the discrete disturbance at 90 Hz.

The following paragraphs describe the operation of the subtraction mode eliminator.

A block diagram of the subtraction eliminator is shown in Figure 2-5. The high-pass filter attenuates the dc component of the input signal before it is fed to the Phase-Lock Loop (PLL) and the Amplitude Control Loop (ACL). The PLL locks onto the largest harmonic within the range of the Voltage-Controlled Oscillator (VCO). For the eliminator, the range of the VCO is 80-110 Hz and the largest harmonic in this range is the discrete disturbance *d(t)* at the ORG's spin speed which is 90 Hz. The output of the VCO is a pure sinusoid at the same frequency as, and in-phase with *d(t)*. The ACL estimates the amplitude of *d(t)*. A reconstruction of *d(t)* is formed by multiplying the output of the ACL with the output of the VCO. This signal is then subtracted from the original input. Feedback nulling forms the basis of operation of the eliminator. With the eliminator's outside loop closed, the differenced signal becomes the eliminator's output, and it is this signal that feeds the PLL and ACL. The outputs of these loops are adjusted via feedback until the elimi-

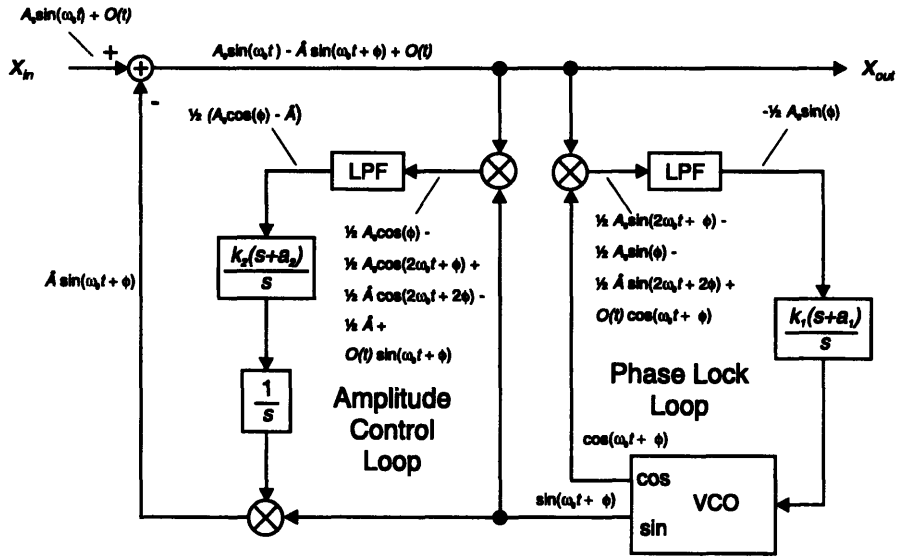

Figure 2-6: Simplified Block Diagram of Subtraction Eliminator with Signals

nator's output no longer contains the largest discrete harmonic within the range of the VCO. In this manner, the eliminator resembles a "notch" at the ORG's spin frequency.

Note: The eliminator as implemented by Doerr contains additional circuitry for automatic control of the gain of the PLL. The high gain mode of the PLL is used solely for signal acquisition. This thesis assumes that the eliminator has acquired and locked onto the discrete disturbance *d(t)*. Therefore, all analysis will be restricted to the PLL in the low-gain mode.

2.2.1 Theory of Operation

The detailed analysis of the signals within the subtraction eliminator was developed by Doerr[2]. This section provides a brief summary of his results.

A simplified block diagram of the subtraction eliminator, along with propagation of signals within the eliminator, is shown in Figure 2-6. For this analysis, assume that the eliminator is in-lock and that the low pass filters (LPF) are perfect. Let the input signal to the eliminator be

$$x_{in(t)} = A_0 \sin(\omega_0 t) + O(t) \tag{2-10}$$

2. See [4], pages 78-84.

where $A_0\sin(\omega_0 t)$ is the discrete component of the input signal and the remainder of the input is lumped into $O(t)$. The purpose of the eliminator is to filter out the $A_0\sin(\omega_0 t)$ component. With the eliminator in-lock, the output of the VCO is a sinusoid at frequency ω_0 that is out of phase with the discrete component by 90° plus an arbitrary phase error ϕ

$$VCO(t) = \cos(\omega_0 t + \phi) \tag{2-11}$$

The VCO output is multiplied with the eliminator output, x_{out}, and passed to the PLL low pass filter. With the perfect filter assumption, the low pass filter passes only the dc component of the signal:

$$PLL_{LPF(t)} = -\frac{1}{2}A_0\sin(\phi) \tag{2-12}$$

The integrator in the PLL compensation will try to drive (2-12) to zero which is accomplished by driving ϕ to zero:

$$\phi \rightarrow 0 \tag{2-13}$$

In a similar manner as above, the output of the ACL low pass filter is a pure dc signal given by

$$ACL_{LPF(t)} = \frac{1}{2}\left(A_0\cos(\phi) - \hat{A}\right) \tag{2-14}$$

The integrator in the ACL compensation will try to drive (2-14) to zero. Since the PLL drives ϕ to zero, $\hat{A}$ must approach A_0, in order for (2-14) to be driven to zero:

$$\hat{A} \rightarrow A_0 \tag{2-15}$$

Once the eliminator has settled so that $\phi \cong 0$ and $\hat{A} \cong A_0$, the output becomes

$$x_{out(t)} \cong O(t) \tag{2-16}$$

The discrete component is removed.

As $x_{out}(t) \rightarrow O(t)$, the signal fed to the PLL no longer has the discrete component of the input signal. Nonetheless, the PLL is able to remain in-lock. This is due to the fact that the PLL integrator acts as a memory function. Even with its input zero, the integrator continues to output the steady-state value that defines the lock condition for the VCO.

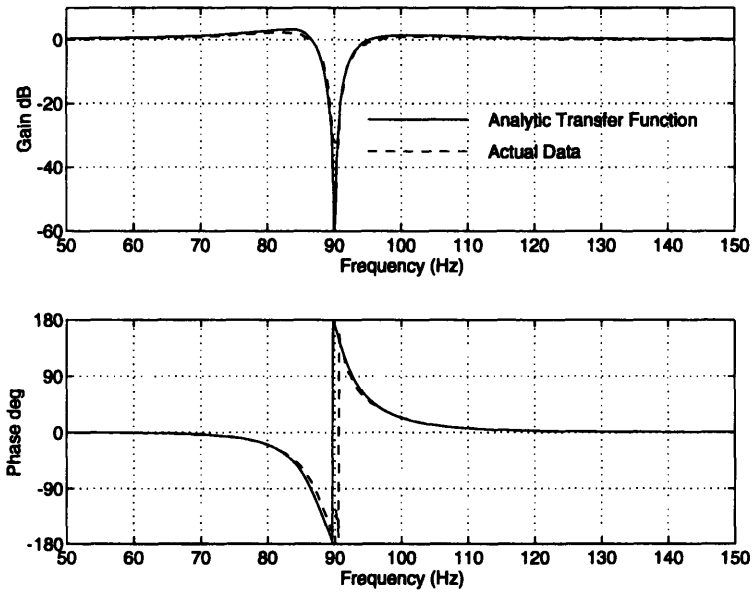

Figure 2-7: Analytic Model Versus Hardware Data for Subtraction Eliminator

2.2.2 Subtraction Eliminator Model

The development of the linear time-invariant model for the subtraction eliminator proceeds as follows. The block diagram of Figure 2-5 is converted into a set of seven nonlinear differential equations. Then, the nonlinear differential equations are linearized to form a linear time-varying model. Finally, the time-varying model is simplified to form a linear time-invariant transfer function which becomes the model for the subtraction eliminator used in the analysis of this thesis. Due to its length, the derivation of the subtraction eliminator model is presented in Appendix A. The subtraction eliminator model, given in Appendix A as Equation (A-68), is rewritten here:

$$E(s) = \frac{(s+100)\,(s^2+200s+3.30\times10^5)\,(s^2+3.20\times10^5)^2}{(s+102)\,(s^2+126s+3.39\times10^5)\,(s^2+30.8s+3.26\times10^5)\,(s^2+41.8s+3.00\times10^5)}\,\frac{V}{V} \qquad (2\text{-}17)$$

Figure 2-7 shows a comparison of (2-17) and hardware test data. It is seen that the above model forms a close match to actual data.

2.3 The Baseline Controller Model

The schematic of the mirror controller, as implemented by Feldgoise, is shown in Figure 2-8. The transfer function for this controller is given by

$$C(s) = \frac{1.19\,(s+101.32)\,(s+100)^2}{s^2\,(s+2130)}\frac{V}{V} \tag{2-18}$$

This controller will be referred to as the *baseline controller.*

2.4 The Mirror Model

The mirror model was obtained by fitting a transfer function to actual test data. The test data represents the open-loop transfer function from the input to the mirror, as a voltage proportional to torque, to the output of the quad detector, as a voltage proportional to the mirror angle. Thus, the mirror model combines the fast steering mirror transfer function $F(s)$, the mirror gain, and the quad detector. The mirror model is given by

$$M'(s) = \frac{1.1411 \times 10^7}{s^2 + 9.192s + 5868}\frac{V}{V} \tag{2-19}$$

A comparison of (2-19) and the test data is shown in Figure 2-9. The mirror model transfer function and the test data agree closely except at the resonant peak. Coherence was low at the resonance, flattening the measured peak.

The mirror model is modified to also include the mirror loop gain k shown in Figure 2-2 where, for the pointing stabilization testbed, $k = 0.05$. Multiplying k with (2-19) gives the modified mirror model

$$M(s) = \frac{5.7055 \times 10^5}{s^2 + 9.192s + 5868}\frac{V}{V} \tag{2-20}$$

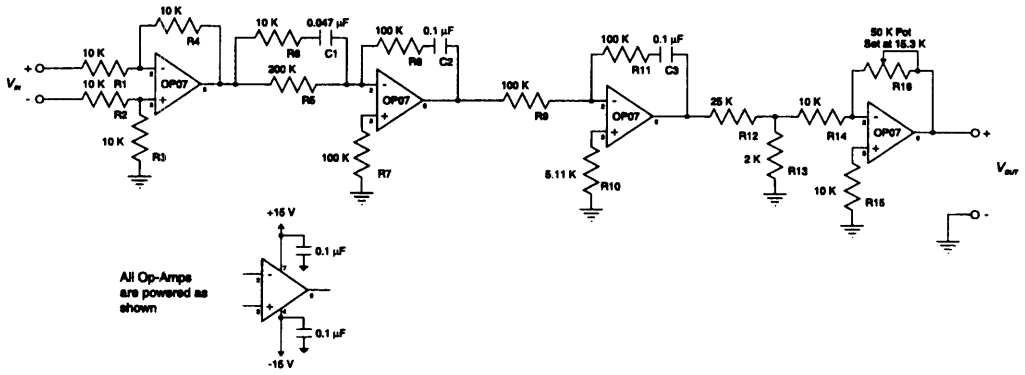

Figure 2-8: Baseline Mirror Controller Schematic

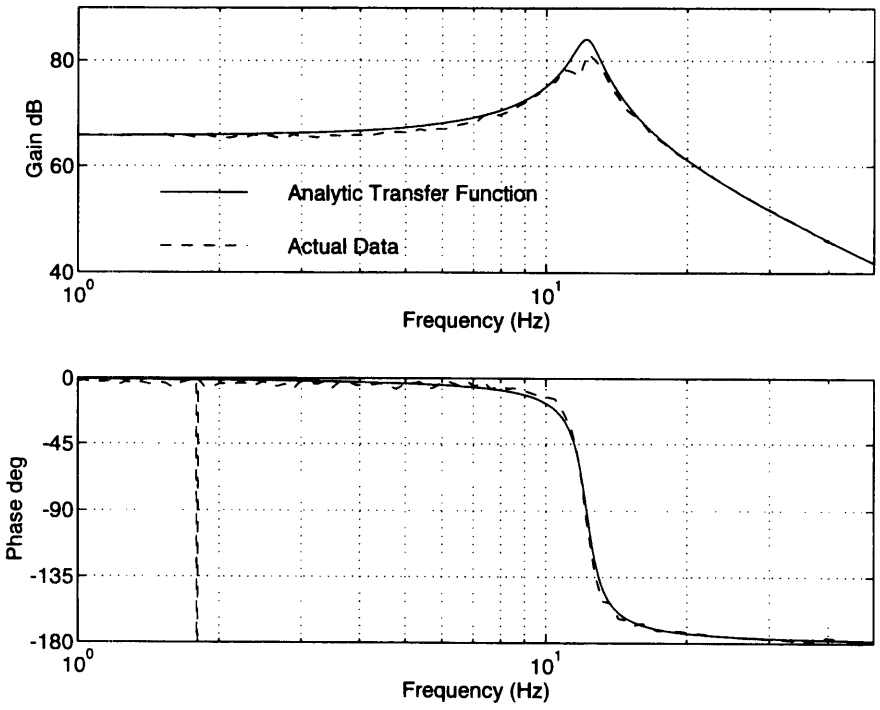

Figure 2-9: Mirror Model Versus Hardware Data

Chapter 3: Subtraction Eliminator Controller Design

This section develops the designs to extend the mirror loop's crossover frequency when the subtraction eliminator is used to cancel the discrete disturbance.

Although the eliminator model given in the previous chapter is seventh order, the dominant behavior of the eliminator can be simplified to a fourth order model. This fourth order model acts as a "double-notch" filter - two complex zero pairs on the $j\omega$-axis at the notch frequency and two complex pole pairs horizontally even with the zeros, but displaced into the left-hand plane. Without loss of generality, Figure 2-7 can be considered the transfer function of a typical double-notch. Notice that the phase of the double-notch is -180° for frequencies immediately below the notch frequency. It is the 180° of phase lag at the notch frequency that causes stability problems when extending the open-loop crossover frequency of the mirror loop beyond the notch frequency.

Three designs that extend the mirror loop crossover beyond the notch frequency and have acceptable stability margins will be discussed in this chapter. The first design cascades a lead compensator to the baseline controller in an attempt to extend the mirror loop bandwidth. This is followed by a controller design based on the linear quadratic regulator (LQR) servo methodology. The final design is based on classical design techniques and uses bode and nyquist plots to alter the baseline controller to achieve a higher open-loop crossover frequency. The phase lag of the eliminator is explicitly taken into account in the first and third designs by use of lead compensation. The LQR design implicitly takes the phase lag into account through the stability guarantee of the LQR method.

3.1 Lead Compensation Controller

The first approach to extending the mirror loop's open-loop crossover frequency with the eliminator in the loop was to add lead compensation to the baseline controller. The nyquist plot of the mirror loop with the baseline controller and a 200 Hz crossover is shown in Figure 3-1, where the baseline controller was only modified by raising the loop gain. Note that without any modifications, this loop is unstable. Over 90° of phase lead is needed to stabilize the system which requires a second order lead compensator. A compensator which provides 140° of phase lead is given by

$$L(s) = \frac{(s+100)^2}{(s+3000)^2} \tag{3-1}$$

The nyquist plot of the mirror loop after adding the lead compensator is shown in Figure 3-2. This loop is stable with a phase margin of 63° at the "notch" crossover. The open-loop transfer function is shown in Figure 3-3. A lead compensator adds gain at high frequency which increases the open-loop crossover. For this design, one with a large amount of phase lead, the open-loop crossover frequency is extended beyond 1 kHz. Such a high crossover frequency is undesirable because of the possibility of exciting unmodeled, high-frequency dynamics of the mirror.

Although this design is stable with 63° of phase margin, the high open-loop crossover frequency prevents the practical implementation of this design.

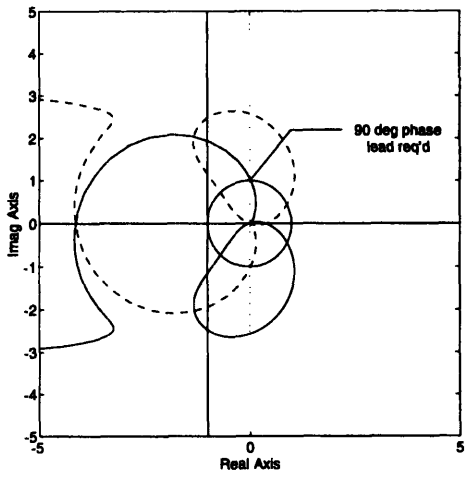

Figure 3-1: Lead Compensator Design Nyquist Plot (Before Lead Compensation)

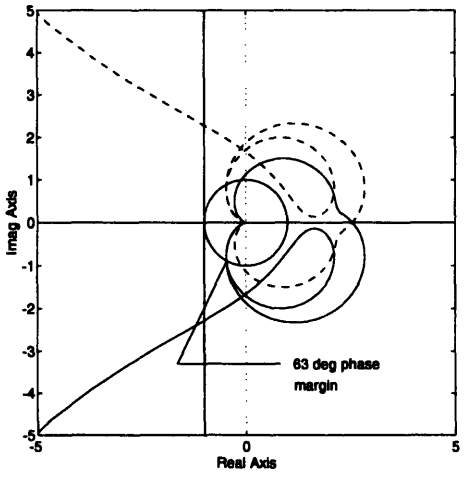

Figure 3-2: Lead Compensation Design Nyquist Plot (After Lead Compensation)

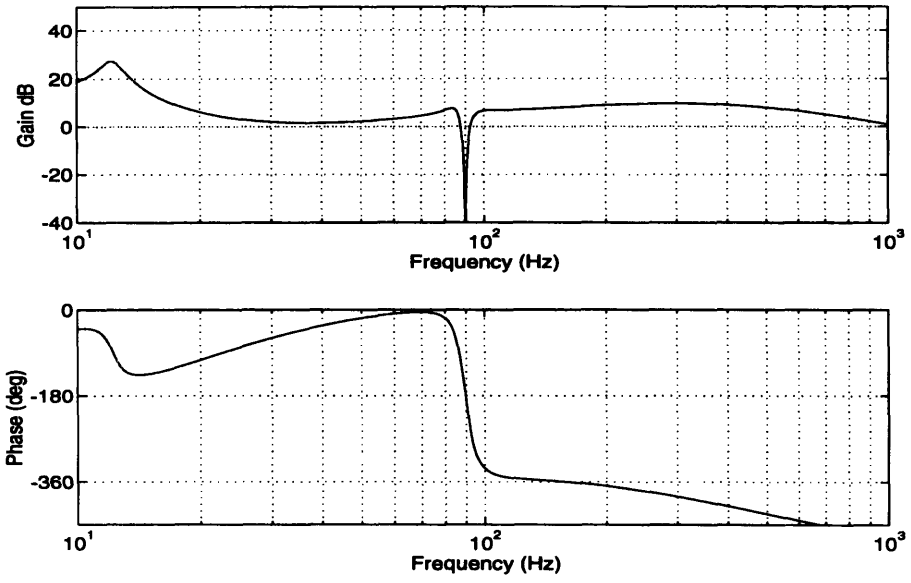

Figure 3-3: Lead Compensator Design - Open Loop Transfer Function

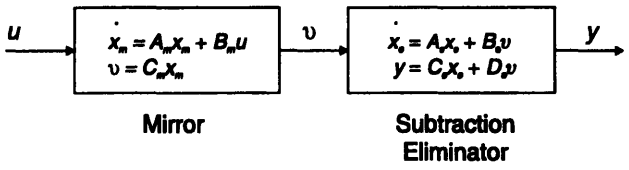

Figure 3-4: Plant Model for LQR Servo Design

3.2 Linear Quadratic Regulator (LQR) Servo Controller

This section discusses the linear quadratic regulator (LQR) servo design methodology [1, 2] applied to the mirror loop. The methodology used here deviates from the original LQR methodology by adding an integrator in the design to provide zero steady-state errors to step inputs. The LQR servo design methodology is applied to linear time-invariant (LTI) state-space systems. A linear optimal controller is developed which minimizes a quadratic cost function. This analysis is specialized to the case of the mirror loop with the eliminator and uses the models for the eliminator and the mirror given in Chapter 2, both converted to state-space form.

3.2.1 LQR Servo Methodology

Let the system plant be composed of the mirror and the subtraction eliminator connected in series as shown in Figure 3-4.

Let the mirror be modeled as

$$\begin{aligned} \dot{x}_m &= A_m x_m + B_m u \\ \upsilon &= C_m x_m \end{aligned} \tag{3-2}$$

where $x_m \in \Re^2$, $u \in \Re^1$, and $\upsilon \in \Re^1$, and A_m, B_m, and C_m are of proper dimension.

Let the LTI eliminator model be given by

$$\begin{aligned} \dot{x}_e &= A_e x_e + B_e \upsilon \\ y &= C_e x_e + D_e \upsilon \end{aligned} \tag{3-3}$$

where $x_e \in \Re^7$, $y \in \Re^1$, and A_e, B_e, C_e, and D_e are of proper dimension.

The only information that will be provided to the controller is the output of the eliminator y. The states x_m and x_e must therefore be estimated via a Kalman filter. The optimal controller design can be completely separated into the design of the deterministic optimal controller (x_m and x_e completely available for feedback) and the design of the Kalman filter.

The development of the optimal controller based on the LQR servo methodology will proceed as follows. First, the optimal controller will be developed with the assumption that perfect state information is available. This controller will be referred to as the *optimal full-state feedback controller.* Then, the Kalman filter will be developed which provides the optimal estimate of x_m and x_e given y. Finally, the overall optimal controller will be constructed by combining the optimal full-state feedback controller with the Kalman filter. This controller will be referred to as the *optimal output feedback controller.*

3.2.1.1 LQR Full-State Feedback Controller

Define an augmented control plant which combines the mirror and the eliminator along with an integrator to achieve zero steady-state error to step inputs. The integrator will later be incorporated into the optimal controller.

The augmented control plant is modeled as

$$\dot{x}_p = A_p x_p + B_p u \tag{3-4}$$

where

$$x_p = \begin{bmatrix} z \\ y \\ x_m \\ x_e \end{bmatrix}, \quad A_p = \begin{bmatrix} 0_{1\times1} & 1 & 0_{1\times2} & 0_{1\times7} \\ 0_{1\times1} & 0_{1\times1} & D_e C_m A_m + C_e B_e C_m & C_e A_e \\ 0_{2\times1} & 0_{2\times1} & A_m & 0_{2\times7} \\ 0_{7\times1} & 0_{7\times1} & B_e C_m & A_e \end{bmatrix}, \quad \text{and}$$

$$B_p = \begin{bmatrix} 0_{1\times1} \\ D_e C_m B_m \\ B_m \\ 0_{7\times1} \end{bmatrix}$$

The augmented plant has dimension $x_p \in \Re^{11}$. Notice that the eliminator output y is considered a state of the augmented control plant and that the integrator state is denoted by z.

The objective is to develop a full-state feedback controller that is optimal in the sense that it minimizes the cost function

$$J = \int_0^\infty (x_p(t)^T Q x_p(t) + ru^2(t))\, dt \tag{3-5}$$

where Q is the positive semidefinite state weighting matrix and r is the positive (definite) control weighting constant. It is assumed that the pair $[A_p, B_p]$ is stabilizable and the pair $[A_p, N]$ is detectable where $Q = N^T N$.[1]

Given these assumptions, the optimal full-state feedback controller is given by

$$u = -Gx_p \tag{3-6}$$

where G is the feedback gain given by

$$G = \frac{1}{r} B_p^T K \tag{3-7}$$

and K is the positive semidefinite solution to the Control Algebraic Ricatti Equation (CARE)

$$0_{10\times 10} = -KA_p - A_p^T K - Q + \frac{1}{r} K B_p B_p^T K \tag{3-8}$$

3.2.1.2 LQR Kalman Filter

A Kalman Filter is required to estimate x_m and x_e given y. An augmented observer plant is formed whose state is the combination of the mirror and eliminator states

$$x_o = \begin{bmatrix} x_m \\ x_e \end{bmatrix}$$

This augmented plant is further modified to include noise dynamics. Assume that there exists a process noise $v \in \Re^1$ that enters the system in the same manner as the control u and that

1. Stabilization requires that all uncontrollable modes be stable while detectability requires that all unobservable modes be stable [3].

there exists a measurement noise $w \in \Re^1$ that adds directly to the output y. Let v and w be uncorrelated, zero-mean white noise processes with covariances

$$\begin{aligned} \text{cov}\left[v(t_1), v(t_2)\right] &= V\delta(t_2 - t_1) \\ \text{cov}\left[w(t_1), w(t_2)\right] &= W\delta(t_2 - t_1) \end{aligned} \tag{3-9}$$

where $V \in \Re^{1x1}$, $W \in \Re^{1x1}$, and $\delta(t)$ is the unit impulse function.

The augmented plant model is then given by

$$\begin{aligned} \dot{x}_o &= A_o x_o + B_o u + Lv \\ y &= C_o x_o + w \end{aligned} \tag{3-10}$$

where

$$A_o = \begin{bmatrix} A_m & 0_{2\times 7} \\ B_e C_m & A_e \end{bmatrix}, \quad B_o = \begin{bmatrix} B_m \\ 0_{7\times 1} \end{bmatrix}, \quad L = B_o, \quad \text{and} \quad C_o = \begin{bmatrix} D_e C_m & C_e \end{bmatrix}$$

Assume that the pair $[A_o, L]$ is stabilizable and that the pair $[A_o, C_o]$ is detectable. Then the Kalman filter for (3-10) is given by

$$\dot{\hat{x}}_o = A_o \hat{x}_o + B_o u + H\left(y - C_o \hat{x}_o\right) \tag{3-11}$$

where

$$H = \Sigma C_o^T W^{-1} \tag{3-12}$$

and Σ is the positive semidefinite solution to the Filter Algebraic Ricatti Equation (FARE)

$$0_{9\times 9} = A_o \Sigma + \Sigma A_o^T + LVL^T - \Sigma C_o^T W^{-1} C_o \Sigma \tag{3-13}$$

3.2.1.3 LQR Output Feedback Controller

The optimal output feedback controller is obtained from the optimal full-state feedback controller by using the state estimate from the Kalman filter in place of the perfect state information assumption. Let the feedback gain determined for the optimal full-state feedback controller be written as

$$G = \begin{bmatrix} G_z & G_y & G_o \end{bmatrix} \tag{3-14}$$

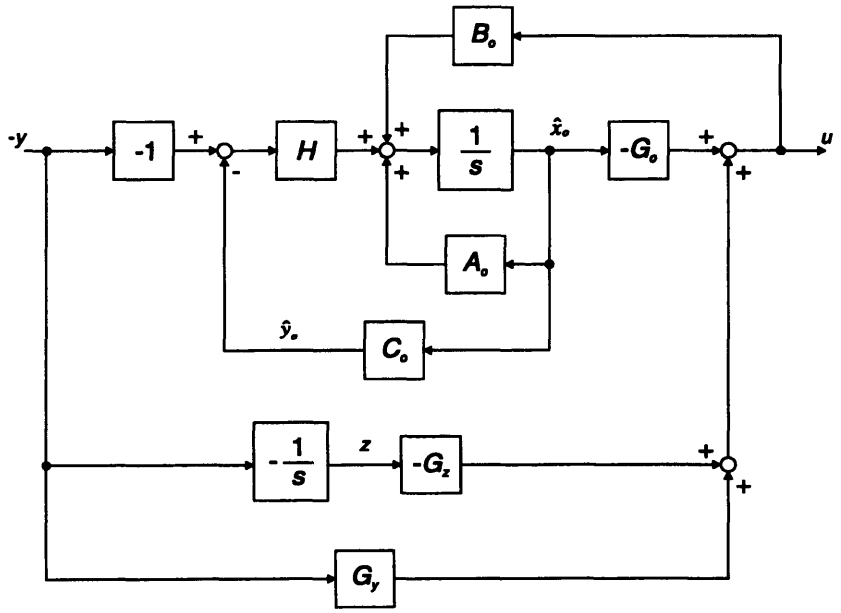

Figure 3-5: Optimal Output Feedback Controller (with Integrator)

where $G_z \in \Re^{1x1}$, $G_y \in \Re^{1x1}$, and $G_o \in \Re^{1x9}$. Then the optimal output feedback controller, shown in Figure 3-5, is modeled as

$$\begin{aligned} \dot{x}_c &= A_c x_c + B_c(-y) \\ u &= C_c x_c + D_c(-y) \end{aligned} \tag{3-15}$$

where the integrator of the augmented control plant is now incorporated into the controller and the matrices A_c, B_c, C_c, and D_c are given by

$$A_c = \begin{bmatrix} A_o - B_o G_o - H C_o & -B_o G_z \\ 0_{1\times 9} & 0_{1\times 1} \end{bmatrix}, \quad B_c = \begin{bmatrix} B_o G_y - H \\ -1 \end{bmatrix},$$

$$C_c = \begin{bmatrix} -G_o & -G_z \end{bmatrix}, \text{ and } D_c = \begin{bmatrix} G_y \end{bmatrix}$$

The stability of the closed-loop system is guaranteed by the LQR methodology provided that the stabilizability and detectability requirements are met.

3.2.2 LQR Servo Design with Eliminator

The LQR servo methodology was applied to the mirror loop with the subtraction eliminator using the models derived in Chapter 2. The parameters V and W were set as follows

$$\begin{aligned} V &= 1 \\ W &= 1 \end{aligned} \tag{3-16}$$

The parameters $Q=N^TN$ and r were adjusted to achieve an open-loop crossover frequency of approximately 200 Hz. The specific values used for the final design were

$$\begin{aligned} N &= \left[2.24\times10^5\ 31.62\ -6.10\ 6.10\ 0\ 0\ 0\ 0\ 0\ 0\ 0\right] \\ r &= 1000 \end{aligned} \tag{3-17}$$

Using these parameters, the optimal output feedback controller is given

$$C(s) = \frac{9.17\left(\begin{array}{c} s^{10}+2.51\times10^3s^9+3.09\times10^6s^8+3.32\times10^9s^7+ \\ 2.38\times10^{12}s^6+1.55\times10^{15}s^5+7.19\times10^{17}s^4+ \\ 3.03\times10^{20}s^3+8.14\times10^{22}s^2+2.05\times10^{25}s+1.48\times10^{27} \end{array}\right)}{\left(\begin{array}{c} s^{10}+4.58\times10^3s^9+6.19\times10^6s^8+5.55\times10^9s^7+ \\ 5.15\times10^{12}s^6+2.28\times10^{15}s^5+1.53\times10^{18}s^4+ \\ 3.52\times10^{20}s^3+1.55\times10^{23}s^2+1.33\times10^{25}s \end{array}\right)} \tag{3-18}$$

The open-loop transfer function is shown in Figure 3-6 and the controller poles are given in Table 3-1. It is seen that an open-loop crossover frequency of 254 Hz has been achieved. The closed-loop system is stable; however, the controller is tenth order with two unstable poles.

Table 3-1

Controller Pole Locations
-2.9267x103
-1.3657x103
-1.0002x102+5.6546x102j
-1.0002x102-5.6546x102j
1.0482x101+5.6208x102j
1.0482x101-5.6208x102j
-1.8954x100+5.6558x102j
-1.8954x100-5.6558x102j
-1.00000x102
0

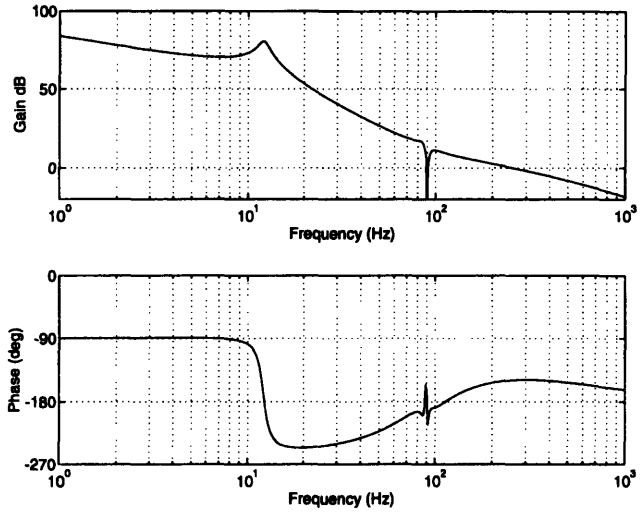

Figure 3-6: LQR Design - Open-Loop Transfer Function

For this application, a tenth order controller tends to be impractical. This controller also tends to be sensitive to errors in the modeling of the plant and eliminator. For example, this design was based on the assumption that the eliminator's notch frequency, that is, the frequency of the discrete disturbance, was 90 Hz. If the frequency of the discrete disturbance happens to be outside the frequency band of 89.5 to 90.8 Hz, then the closed-loop system becomes unstable.

3.3 Classical Controller Design

The third design method employed nyquist and bode plots of the mirror loop along with some trial and error. The controller design began with two integrators to provide low-frequency attenuation and zero steady-state errors to ramp inputs. These two poles result in a phase of -180°. A real-axis zero was added to bring the phase up to -90°. Next, a complex pair of zeros were added to approximately cancel the poles of the mirror. Then, a first order lead compensator was added to adjust the phase in the eliminator's "notch" region. Finally, a high-frequency pole was added to make the controller proper. The complex zeros and the high-frequency pole were adjusted to improve the phase margin of the design. The final controller design is given by

$$C(s) = \frac{21.26\,(s^2 + 20s + 6500)\,(s + 120)\,(s + 126)}{s^2\,(s + 2530)\,(s + 4000)} \tag{3-19}$$

The phase margin of this design is limited by the 0 dB crossover of the "notch." From the nyquist plot of Figure 3-7, the phase margin is shown to be 28°. The open-loop transfer function of the mirror loop (Figure 3-8) shows that the crossover frequency of this design is 210 Hz.

This design is stable, fourth order and practicable to implement. The open-loop crossover frequency can be raised by increasing the loop gain, neglecting unmodeled dynamics. This design has the disadvantages of a small phase margin as well as a low slope at crossover which increases the sensitivity of the crossover frequency to loop gain. Another disadvantage, one inherent to lead compensation designs, is that the loop gain is reduced at low frequencies resulting poorer low-frequency disturbance rejection.

3.4 Eliminator Controller Design: Conclusion

Both the controller design based on adding lead compensation to the baseline controller and the LQR servo design method are not practical for implementation and thus not pursued further. The classical controller design given in (3-19) looks promising even though there might be some sacrifice to low-frequency disturbance rejection. This controller design was constructed and tested in the pointing stabilization testbed.

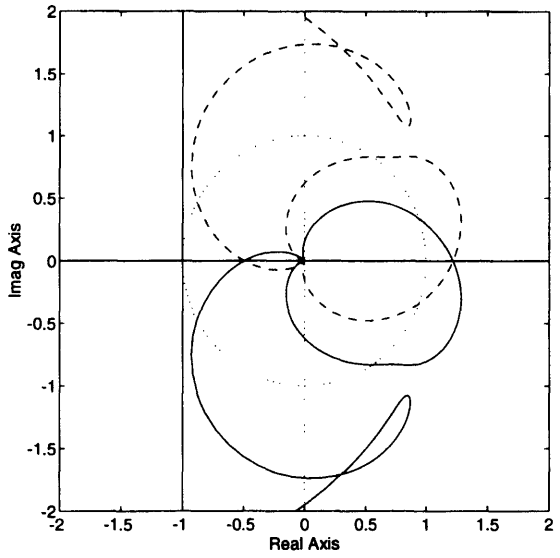

Figure 3-7: Classical Design - Nyquist Plot

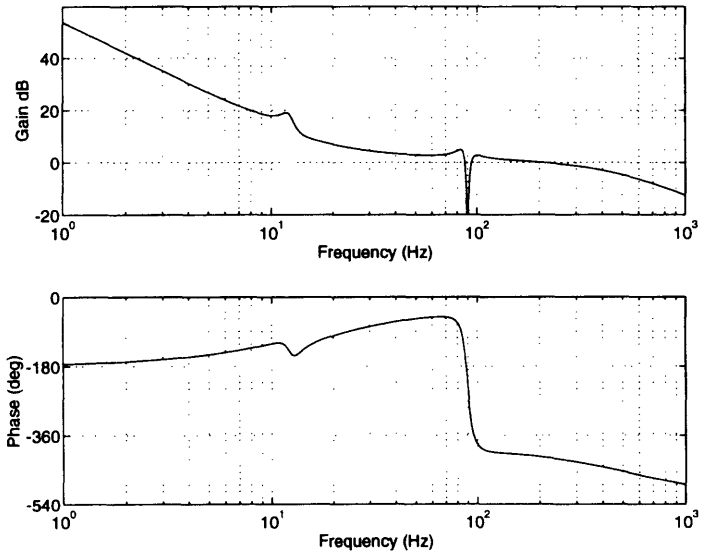

Figure 3-8: Classical Design - Open-Loop Transfer Function

Chapter 4: Notch Controller

In the previous chapter, an analogy between the eliminator and a double-notch filter was made. In this chapter, an single, i.e. second-order, linear notch filter will be considered as an alternative to the eliminator. The advantages of the eliminator are

- The eliminator provides for a very good attenuation of the ORG's spin speed discrete disturbance.
- The eliminator is able to search for and lock onto the discrete disturbance, thereby dynamically controlling the eliminator's notch frequency.

The disadvantages of the eliminator include

- The loop gains of the PLL and ACL are functions of the amplitude of the discrete disturbance. This causes the pole locations to shift as the discrete disturbance's amplitude changes.
- The phase characteristic of the eliminator undergoes a $\pm 180°$ phase change around the notch frequency causing stability problems for higher bandwidth mirror loops.

The second-order linear notch filter, on the other hand, exhibits stable pole/zero locations and only a ±90° phase change around the notch frequency. These characteristics make it easier to design a controller for the notch filter that extends the mirror loop crossover frequency as compared to the eliminator. The disadvantage of the linear notch filter is that the notch frequency is fixed. The unmodified linear filter is unable to search for the discrete disturbance; however, this capability can be incorporated into the notch filter by adding additional circuitry which dynamically controls the notch frequency.

This chapter begins by describing the state-variable design for the linear notch filter and is followed by a discussion of the control circuitry that allows the notch filter to search for and lock onto the discrete disturbance. Next, a lead compensator design to extend the mirror loop crossover frequency is discussed. The chapter concludes with a performance comparison between the eliminator design and the notch filter design.

4.1 The Tracking Notch Filter

The transfer function of a linear second-order notch filter is given by

$$N(s) = \frac{s^2 + \omega_o^2}{s^2 + 2as + (\omega_o^2 + a^2)} \tag{4-1}$$

where ω_o is the notch frequency and a determines the width of the notch. The state-variable implementation of (4-1) is shown in Figure 4-1. The transfer function of a second-order notch filter is shown in Figure 4-2 where $\omega_0 = 2\pi\,(90\text{ Hz})$ and $a = 20$.

4.1.1 Automatic Frequency Control of the Notch Filter

The frequency of the notch filter can be dynamically adjusted by modifying the state-variable block diagram of Figure 4-1. Figure 4-3 shows the modification to the block diagram where A_f is used to adjust the notch frequency. The transfer function of Figure 4-3 is given by

$$N(s) = \frac{s^2 + 32,500A_f}{s^2 + \frac{200}{k+1}s + \frac{1}{k+1}325,000 + \frac{k}{k+1}32,500A_f} \tag{4-2}$$

The notch frequency, in Hz, is given by $f_N = \sqrt{32,500A_f}/(2\pi)$ where A_f is nominally equal to ten.

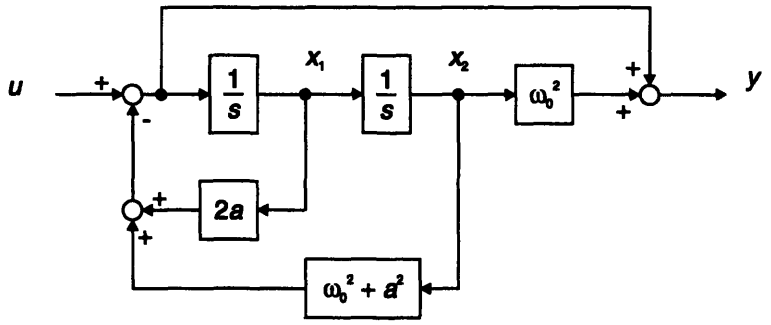

Figure 4-1: State-Variable Implementation of the Second Order Notch

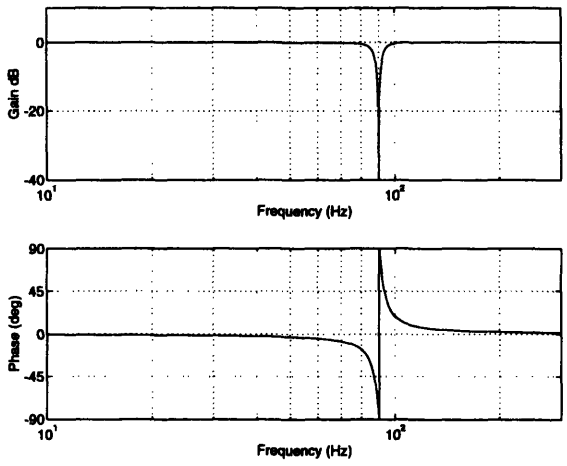

Figure 4-2: Notch Filter Transfer Function

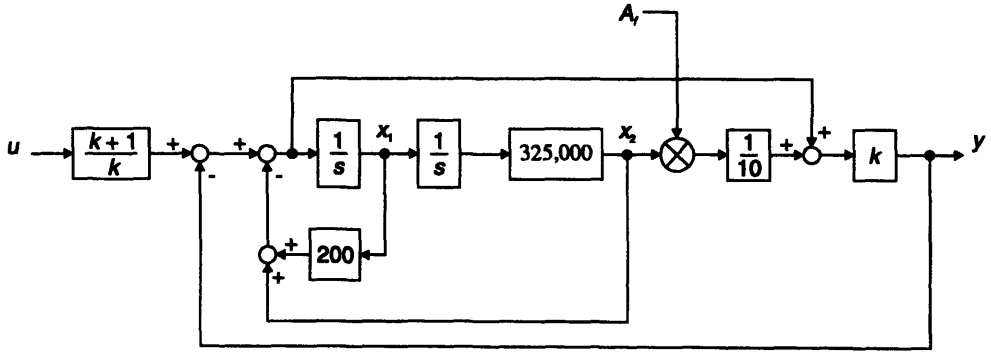

Figure 4-3: Adjustable Frequency Notch Filter Block Diagram

The loop gain k adjusts the value of the s-term in the denominator and thus, the width of the notch. For this design, $k = 4$ which gives a -3 dB width of 7 Hz. The input gain block is included to make the dc and the high-frequency gain equal to one.

The block diagram has been slightly altered to consolidate the x_2 feedback and feedforward gains so that the poles of the notch will move with the zeros. In this configuration, the poles will not be exactly horizontal with the zeros on the s-plane, but this has negligible effect on the transfer function when the s-term of the denominator is much less than the constant term, i.e., $\frac{200}{k+1} \ll 325,000$.

4.1.2 Theory of Operation

The value of A_f is adjusted based on the information provided by the phase of the notch filter transfer function. The input signal to the notch is primarily composed of the discrete disturbance. Therefore, for the discussion that follows, it is assumed that the input signal is a pure sinusoid. By comparing the phase shift of the signal as it passes through the notch, information is obtained on the relative location of the notch frequency and the frequency of the discrete disturbance.

Consider the transfer function of the notch filter shown in Figure 4-2. If the notch frequency is higher than the frequency of the discrete disturbance, then the relative phase between the output of the notch and the input will be negative and A_f should be lowered. If the notch frequency is lower than that of the discrete disturbance, then the relative phase shift will be positive and A_f should be raised.

But first, a mechanism for measuring the phase shift is required. Since the input signal is assumed to be a pure sinusoid, a multiplier followed by a low pass filter can be used for phase detection. But for this type of phase detector to work, one of the input signals must first be shifted by 90°. A phase-lock loop is used in the design to provide the input phase shift.

The notch frequency control mechanism is shown in Figure 4-4. This design is comprised of two control loops - a *Phase-Lock Loop* (PLL) and a *Frequency Control Loop* (FCL). Figure 4-4 also shows the propagation of the signals through the controllers which is explained below.

Let the input signal to the notch filter be the discrete disturbance given by

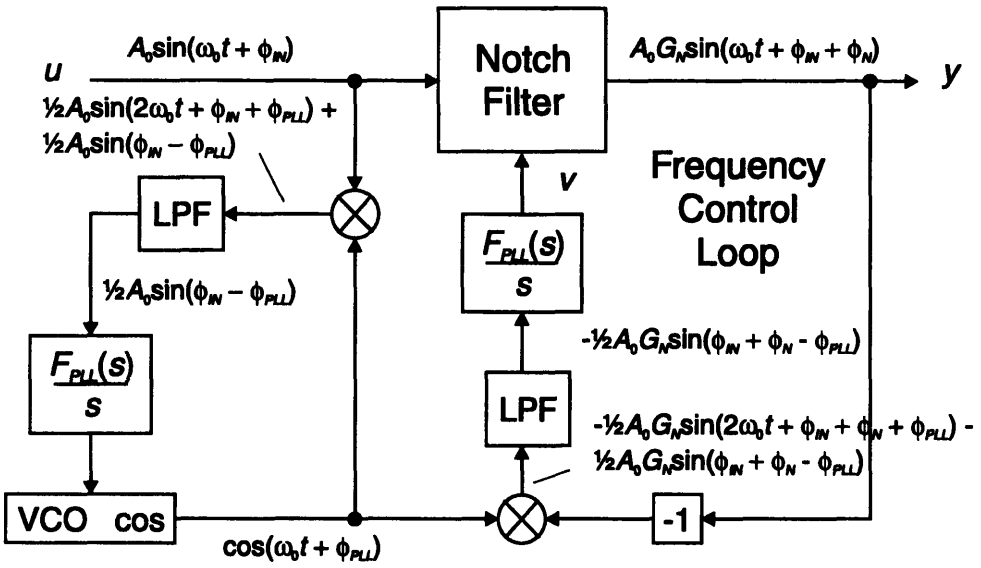

Figure 4-4: Block Diagram of the Frequency Control Mechanism for the Notch Filter

$$u(t) = A_0 \sin(\omega_0 t + \phi_{IN}) \tag{4-3}$$

When the PLL is in-lock, the output of the VCO is 90° out of phase with the input and is given by

$$VCO(t) = \cos(\omega_0 t + \phi_{PLL}) \tag{4-4}$$

where ϕ_{PLL} is the phase shift of the PLL.

The output of the PLL phase detector is the product of (4-3) and (4-4):

$$\begin{aligned} PLL_{PD}(t) &= A_0 \sin(\omega_0 t + \phi_{IN}) \cos(\omega_0 t + \phi_{PLL}) \\ &= \frac{1}{2}A_0 \sin(2\omega_0 t + \phi_{IN} + \phi_{PLL}) + \frac{1}{2}A_0 \sin(\phi_{IN} - \phi_{PLL}) \end{aligned} \tag{4-5}$$

and after the low pass filter attenuates the $2\omega_0$ frequency component, the signal becomes

$$PLL_{LPF}(t) = \frac{1}{2}A_0 \sin(\phi_{IN} - \phi_{PLL}) \tag{4-6}$$

Since the phase error, $\phi_{PLL} - \phi_{IN}$, tends to be small when the PLL is in-lock, (4-6) can be approximated by

$$PLL_{LPF}(t) = \frac{1}{2}A_0(\phi_{IN} - \phi_{PLL}) \tag{4-7}$$

The integrator in the PLL compensator will drive (4-7) to zero so that

$$\phi_{PLL} \rightarrow \phi_{IN} \tag{4-8}$$

so that the VCO phase error equals the input phase.

To examine the signals in the FCL, assume that the notch frequency is set so that the transfer function of the notch filter evaluated at the frequency of the discrete disturbance, i.e., at $s = j\omega_0$, is given by

$$N(j\omega_0) = G_N e^{j\phi_N} \tag{4-9}$$

The output of the notch filter then becomes

$$y(t) = A_0 G_N \sin(\omega_0 t + \phi_{IN} + \phi_N) \tag{4-10}$$

This signal is multiplied by the VCO signal so that the output of the FCL phase detector is

$$\begin{aligned} FCL_{PD}(t) &= -A_0 G_N \sin(\omega_0 t + \phi_{IN} + \phi_N)\cos(\omega_0 t + \phi_{PLL}) \\ &= -\frac{1}{2}A_0 G_N \sin(2\omega_0 t + \phi_{IN} + \phi_N + \phi_{PLL}) - \frac{1}{2}A_0 G_N \sin\left(\phi_{IN} + \phi_N - \phi_{PLL}\right) \end{aligned} \tag{4-11}$$

The low pass filter passes only the dc component of (4-11) so that its output is given by

$$FCL_{LPF}(t) = -\frac{1}{2}A_0 G_N \sin\left(\phi_{IN} + \phi_N - \phi_{PLL}\right) \tag{4-12}$$

Since ϕ_{PLL} approaches ϕ_{IN} by (4-8), (4-12) simplifies to

$$FCL_{LPF}(t) = -\frac{1}{2}A_0 G_N \sin(\phi_N) \tag{4-13}$$

It is this signal that is used to adjust A_f. The integrator in the FCL compensation will drive (4-13) to zero:

$$G_N \sin(\phi_N) \rightarrow 0 \tag{4-14}$$

Figure 4-5 is a plot of $G_N \sin(\phi_N)$ versus the notch frequency obtained analytically by assuming the discrete disturbance frequency is $\omega_o = 2\pi(90\text{ Hz})$. This figure shows that in order for $G_N \sin(\phi_N) \rightarrow 0$, the notch frequency must approach the frequency of the discrete disturbance

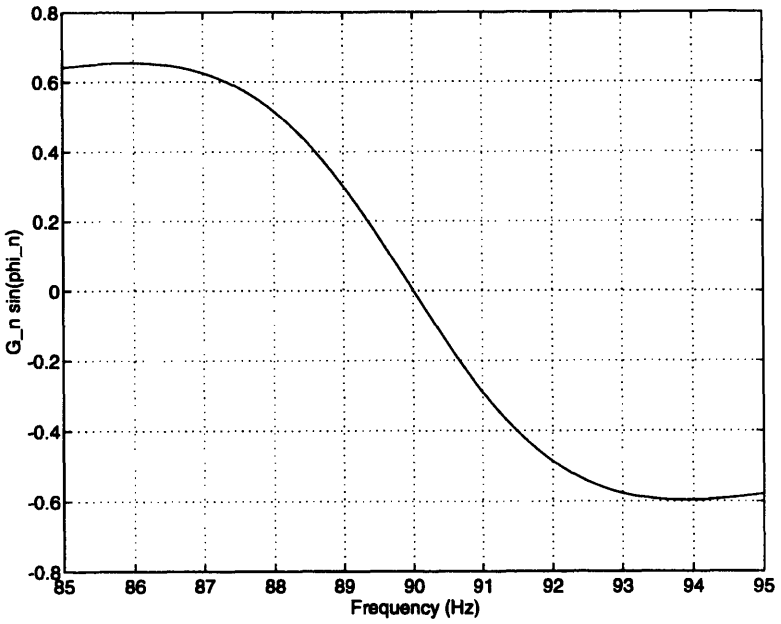

Figure 4-5: $G_N \sin(\phi_N)$ versus Notch Frequency

$$\omega_{Notch} \rightarrow \omega_o \tag{4-15}$$

The desired result is obtained - the notch frequency eventually locks onto the discrete disturbance.

4.1.3 Phase-Lock Loop and Frequency Control Loop Designs

With the addition of the automatic frequency controller, the notch filter is no longer linear. To account for this, the frequency controller is designed to operate at a very low frequency so that the notch frequency does not change rapidly. This allows the notch filter to be considered fixed and linear over short spans of time.

The block diagram of the PLL design is shown in Figure 4-6. A linear representation of the PLL can be obtained by forming a system in which the phase of the discrete disturbance and VCO are the input and output respectively. Equation (4-7) allows the multiplication block to be

modeled by a subtraction block followed by a gain of $\frac{1}{2}A_0$. Figure 4-7 shows the linear representation of the PLL design given that $A_0 = 5$ V. The open-loop bandwidth of this design is 6 Hz.

The block diagram of the FCL design is shown in Figure 4-8. The linear representation of this loop is obtained in a similar manner as for the PLL except that the input is zero and the output is $G_N\sin(\phi_N)$. Equation (4-13) shows that the multiplication block can again be replaced with a subtraction block followed by a gain of $\frac{1}{2}A_0$. Figure 4-9 shows the linear representation of the FCL design. The final gain block represents a linear approximation to the curve $G_N\sin(\phi_N)$ versus A_f. The value of -1.438 represents the slope of the curve where it intersects the line $G_N\sin(\phi_N) = 0$. This curve is derived in a similar manner as that of Figure 4-5 and is of similar shape. The open-loop crossover frequency of this design is 0.22 Hz.

4.2 The Notch Filter Controller

The mirror and the mirror controller together have a phase of approximately -135° at the notch frequency, i.e. at the frequency of the discrete disturbance. Since the notch filter will add 90° of phase lag to the system at this frequency, the closed-loop system will be unstable. A lead compensator is added to the baseline controller to provide 45° of phase lead at the notch frequency. This lead compensator is given by

$$L(s) = \frac{6.78\,(s + 177)}{s + 1064} \tag{4-16}$$

where the constant multiplier is used to adjust the loop gain for a 200$^+$Hz open-loop crossover frequency.

The open-loop transfer function of the mirror loop with the notch filter and the lead compensator added to the baseline controller is shown in Figure 4-10. The phase margin of this design is 33° and is limited by the notch filter crossover. The open-loop crossover frequency is 230 Hz.

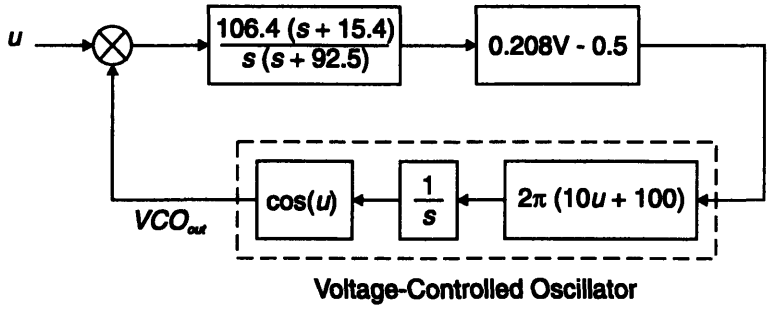

Figure 4-6: Block Diagram of the Phase-Lock Loop Design

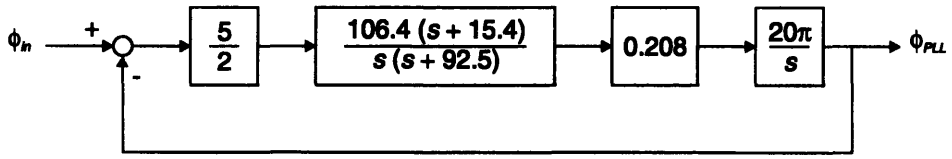

Figure 4-7: Linear Representation of the Phase-Lock Loop Design

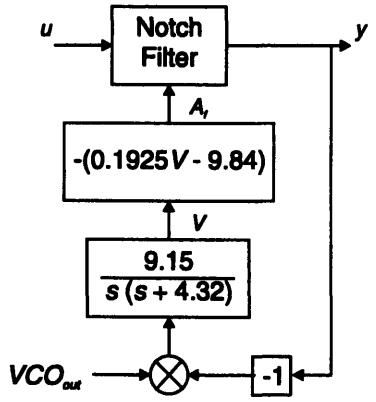

Figure 4-8: Block Diagram of the Frequency Control Loop Design

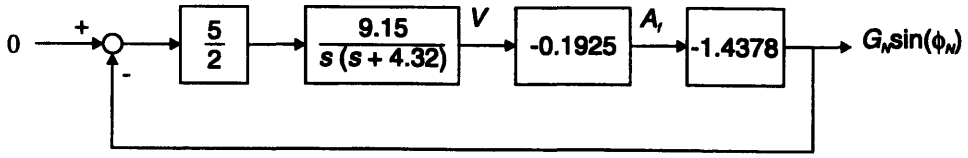

Figure 4-9: Linear Representation of the Frequency Control Loop Design

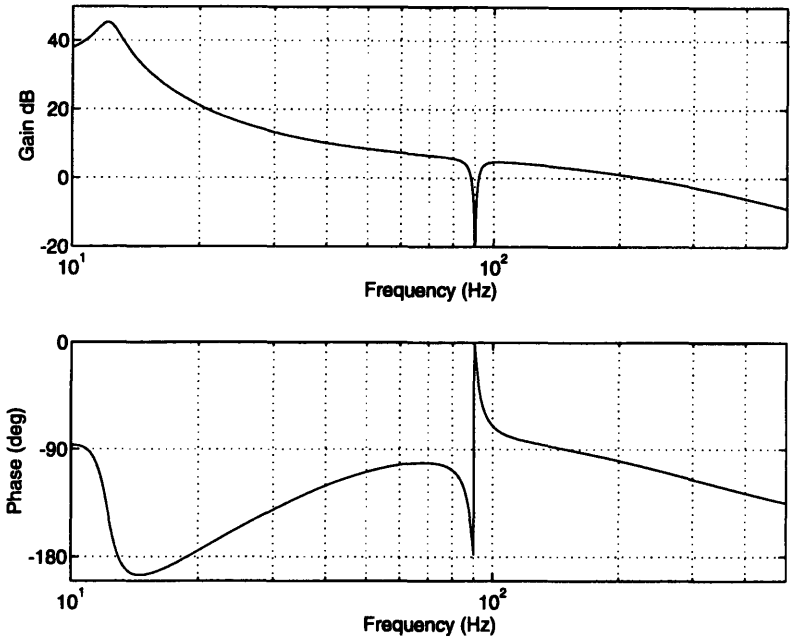

Figure 4-10: Notch Filter Controller - Open-Loop Transfer Function

4.3 Comparison of the Eliminator and the Notch Controller

The sensitivity plots of the eliminator and notch filter designs, both with an open-loop crossover frequency of approximately 200 Hz, are shown in Figure 4-11. The baseline design is that developed by Feldgoise with an open-loop crossover frequency of 60 Hz. For the classical eliminator design, although it offers better attenuation near 90 Hz, the low-frequency attenuation is 10 dB worse than the baseline design. The notch filter design, on the other hand, offers comparable low-frequency performance to the baseline design and improved attenuation in the frequency band of 20 to 300 Hz. Note that because there is a notch in the open-loop, the sensitivity function peaks near the notch frequency.

Overall, considering the frequency band up to 200 Hz, the notch filter design performs better than both the baseline design and the eliminator design.

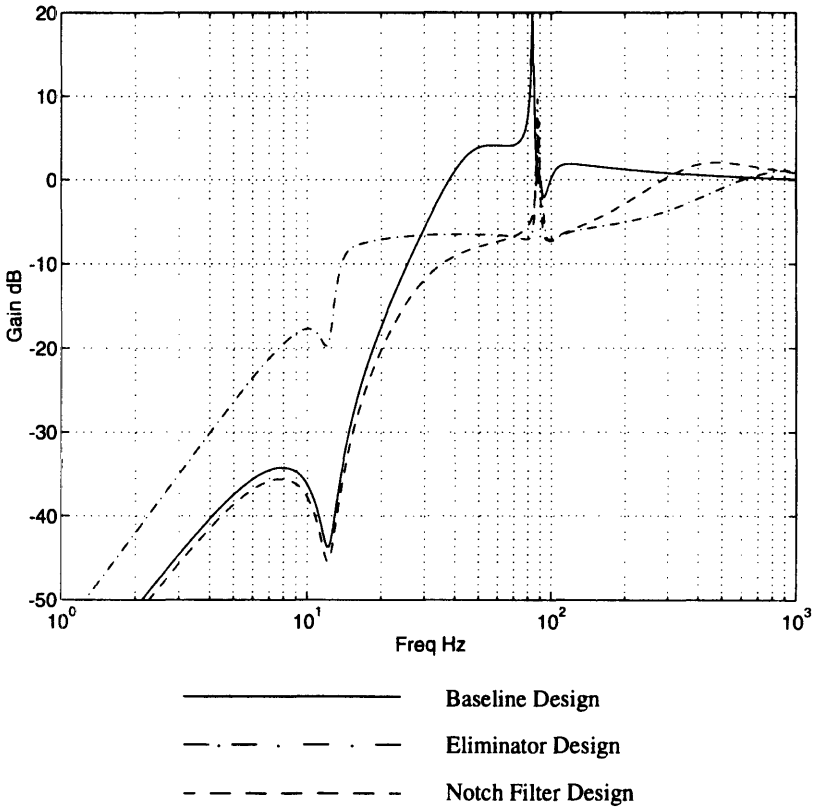

Figure 4-11: Sensitivity Plots of the Eliminator and Notch Filter Designs

Chapter 5: Hardware Implementation and Testing

This chapter describes the hardware implementation of the classical eliminator controller design and the notch filter design, and the subsequent testing of these designs in the mirror loop of the pointing stabilization testbed.

5.1 The Classical Eliminator Controller Design

The classical eliminator controller given in (3-19) was implemented as shown in the schematic diagram of Figure 5-1. Using the actual component values shown in this figure, the eliminator controller transfer function becomes

$$C(s) = \frac{21.37\,(s^2 + 36s + 6670)\,(s + 121)\,(s + 127)}{s^2\,(s + 2620)\,(s + 4010)} \tag{5-1}$$

This controller replaces the baseline controller in the pointing stabilization testbed.

The open-loop transfer function of the mirror loop was obtained using the test setup shown in Figure 5-2. An HP-3562A Dynamic Signal Analyzer was used to generate the test signal and to

produce the open-loop transfer function. The HP_IN and HP_OUT signals were the inputs to the analyzer. The HP-3562A measures the transfer function from HP_IN to HP_OUT which, in this configuration, results in the open-loop transfer function of the mirror loop. The test signal was a sine wave that was swept down from 300 Hz to 10 Hz. The voltage level of the test signal ranged from 5-100 mV. The voltage level was raised to achieve good coherence between the HP_IN and HP_OUT signals, but lowered to 5 mV in the 80 to 100 Hz region to prevent the eliminator from locking onto the test signal.

Figure 5-3 shows a comparison of the open-loop transfer function using simulation and test data. The test data matches well with the simulation data with a slight difference at the mirror resonance frequency where coherence was low. The open-loop crossover frequency of the hardware system was 240 Hz compared to the 210 Hz predicted by the simulation. The difference in crossover frequency can be attributed to the low slope at crossover and thus the actual crossover frequency is quite sensitive to loop gain. The phase margin was measured to be 42°.

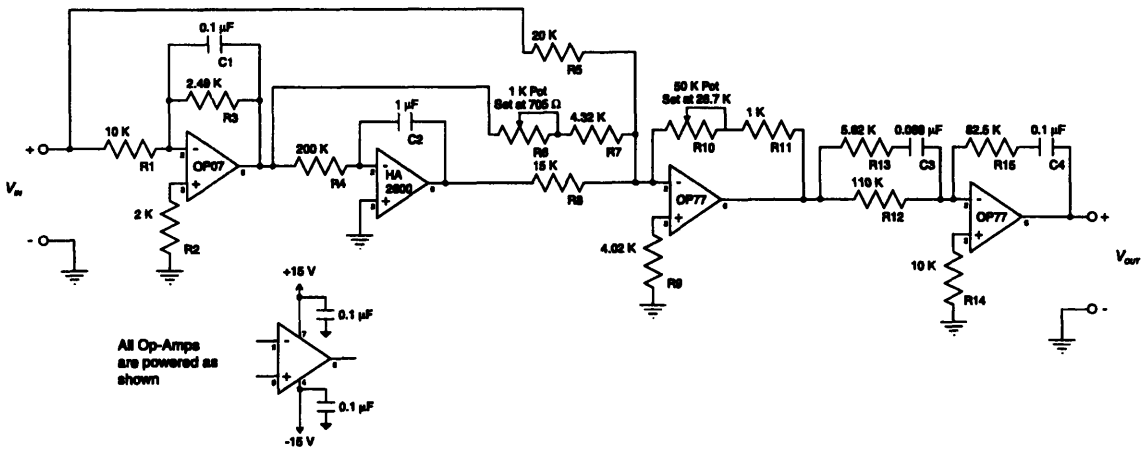

Figure 5-1: Eliminator Controller Schematic

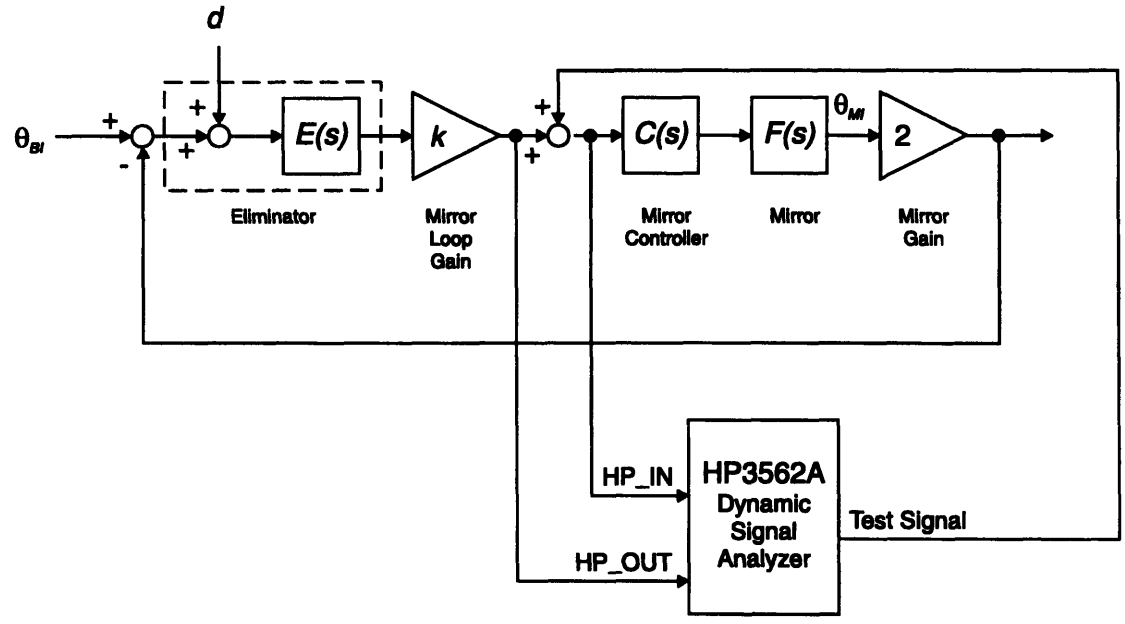

Figure 5-2: Test Setup for Measuring Open-Loop Transfer Function

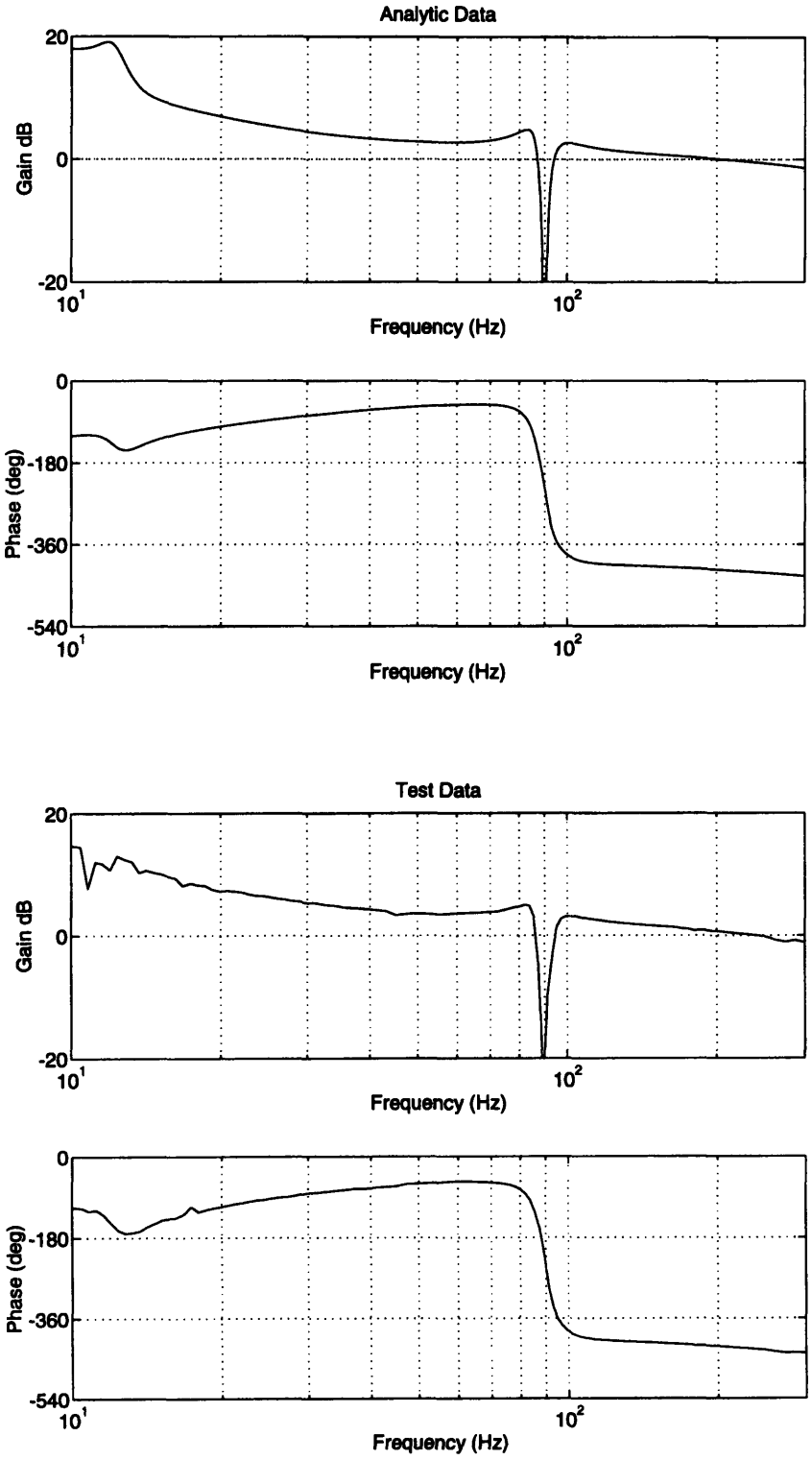

Figure 5-3: Eliminator Controller Design - Open-Loop Transfer Function

5.2 The Tracking Notch Filter and Notch Filter Controller Designs

The notch filter design is composed of two parts - the tracking notch filter which includes the automatic frequency control logic and the notch filter controller.

5.2.1 The Tracking Notch Filter

The block diagram of the tracking notch filter is shown in Figure 5-4. The tracking notch filter is made up of an adjustable frequency linear notch filter and an automatic frequency controller. The block diagram of the adjustable frequency linear notch filter is shown in Figure 5-5. This filter has an input u, an output y, and an additional input, v, to control the notch frequency. With v held constant, the notch filter is linear time-invariant. The notch frequency can be adjusted between 80-100 Hz as v is varied from -12 to 12 V. A schematic diagram of the linear notch filter is shown in Figure 5-6.

The automatic frequency controller is composed of two parts: the Phase-Lock Loop (PLL) and the Frequency Control Loop (FCL). The block diagram of the PLL is shown in Figure 5-7 and the schematic diagram is shown in Figure 5-8. The frequency range of the PLL is 80-120 Hz and the PLL will lock onto the largest discrete of the input signal in this frequency range. The Voltage-Controlled Oscillator (VCO) is implemented externally using an HP3314A Signal Generator. The output of the PLL is the output of the VCO.

The block diagram of the FCL is shown in Figure 5-9. The inputs to the FCL are the output of the notch filter and the output of the VCO. The output of the FCL is the signal v which is used to adjust the notch frequency. The schematic diagram of the FCL is shown in Figure 5-10.

Due to imperfections of the of the two integrators of the notch filter, an adjustment to the design was made to improve the attenuation in the notch region. This adjustment is shown as the dotted path in the notch filter block diagram and the gain of this path was adjusted to maximize the notch depth at 90 Hz. With the automatic frequency control circuitry disabled, the notch filter's attenuation at 90 Hz was measured to be -80 dB with the notch set manually to 90 Hz, and the attenuation at 88 and 92 Hz were -60 dB with the notch is set to 88 and 92 Hz, respectively. With the automatic frequency controller enabled, the notch filter exhibited approximately 55 dB of attenuation at the depth of the notch. This level of attenuation is comparable to that of the elimina-

tor and remained stable as the lock signal was varied over a frequency range of 85-95 Hz. The settling time for the frequency control circuitry was on the order of 5-10 seconds.

5.2.2 The Notch Filter Controller

The notch filter controller was implemented as a simple modification to the baseline controller. These changes are circled in Figure 5-11. The series resistor R17 and capacitor C4 were added to implement the lead compensator while the resistor R16 was raised to adjust the open-loop crossover frequency. The test setup of Figure 5-2 was modified by replacing the eliminator with the tracking notch filter and modifying the baseline controller to include the lead compensator. A comparison of the open-loop transfer functions obtained from simulation and from test data is shown in Figure 5-12. The two transfer functions match well. The open-loop crossover frequency is 212 Hz and the phase margin is 23°, compared to the simulation prediction of 230 Hz and 33°, respectively. However, the ORG noise at 270 Hz and 556 Hz is more significant when compared to the baseline design. This is to be expected considering the higher open-loop gains at these frequencies for the notch filter design.

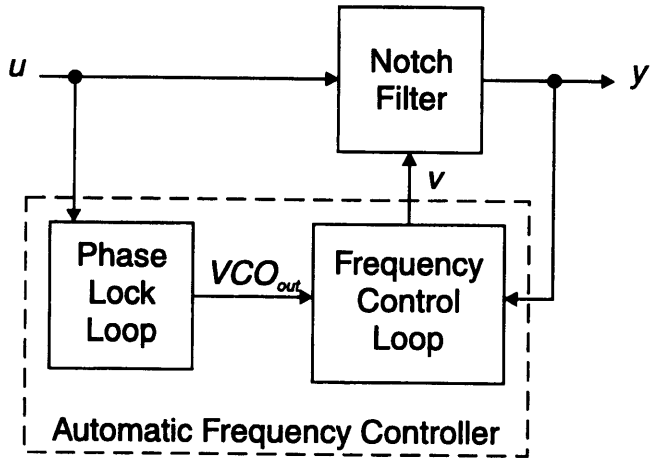

Figure 5-4: Tracking Notch Filter Block Diagram

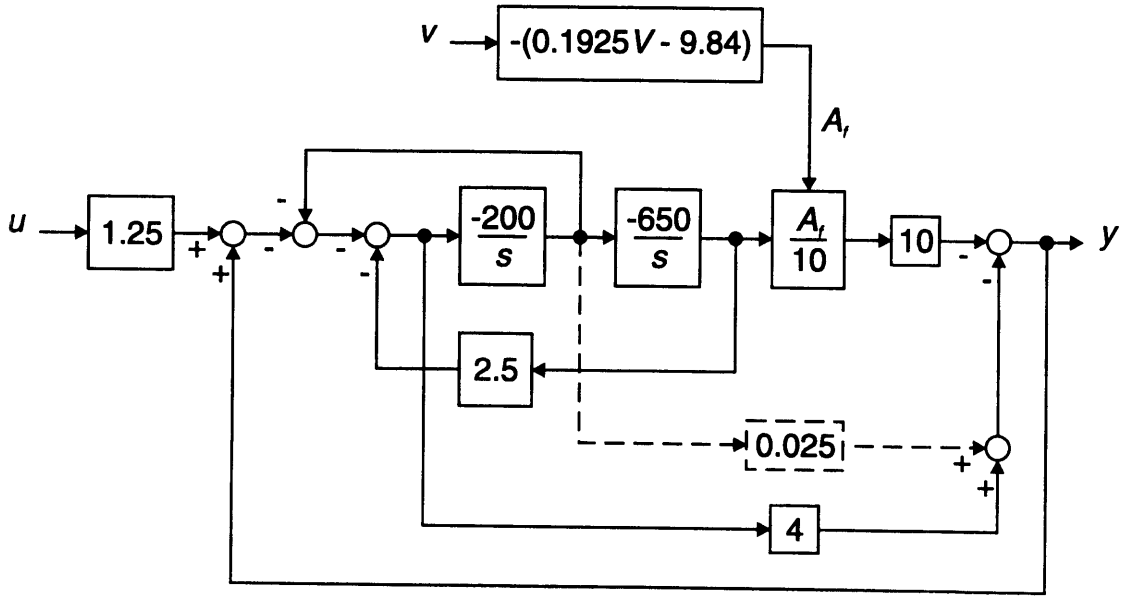

Figure 5-5: Notch Filter Block Diagram

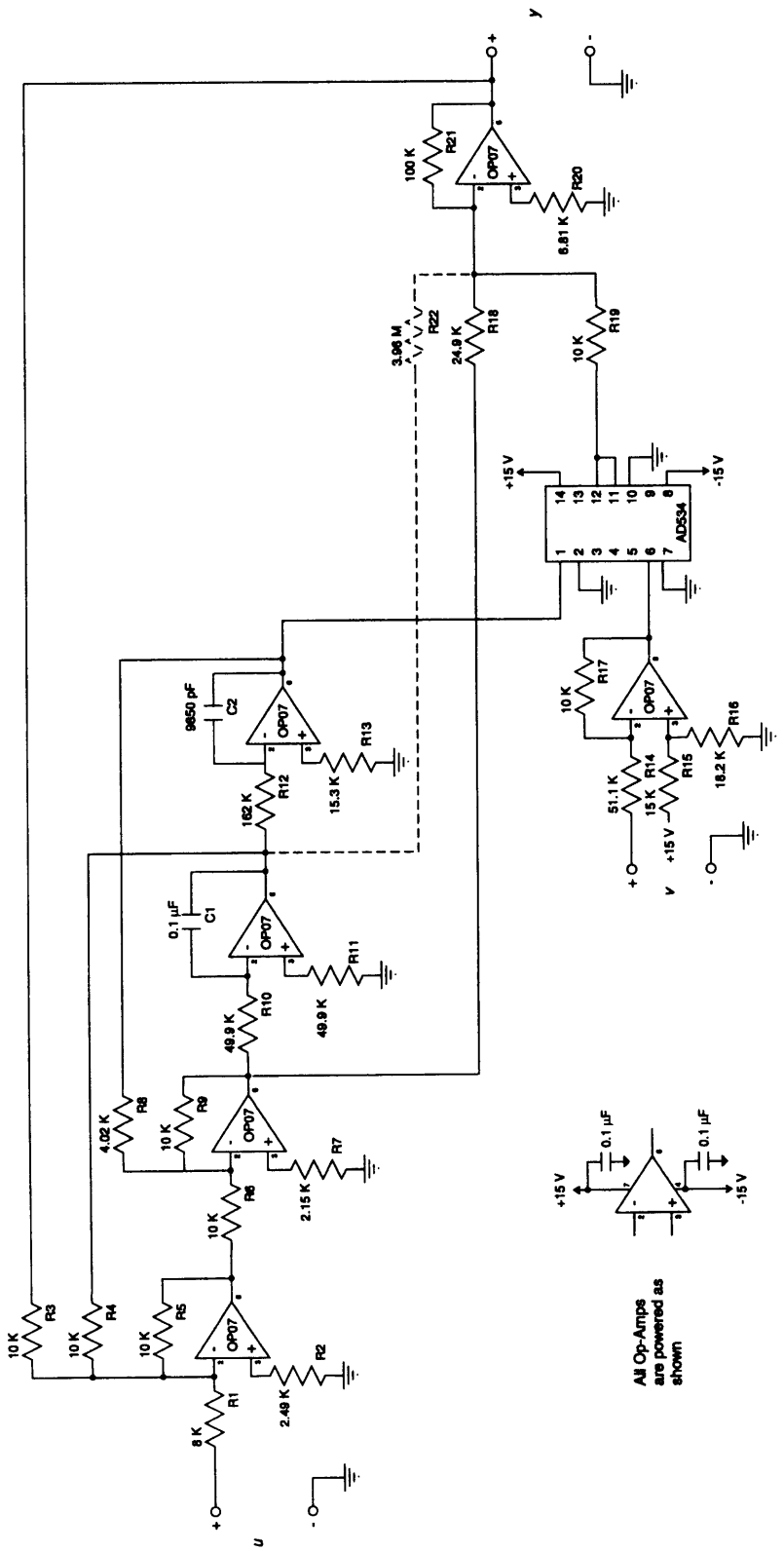

Figure 5-6: Notch Filter Schematic Diagram

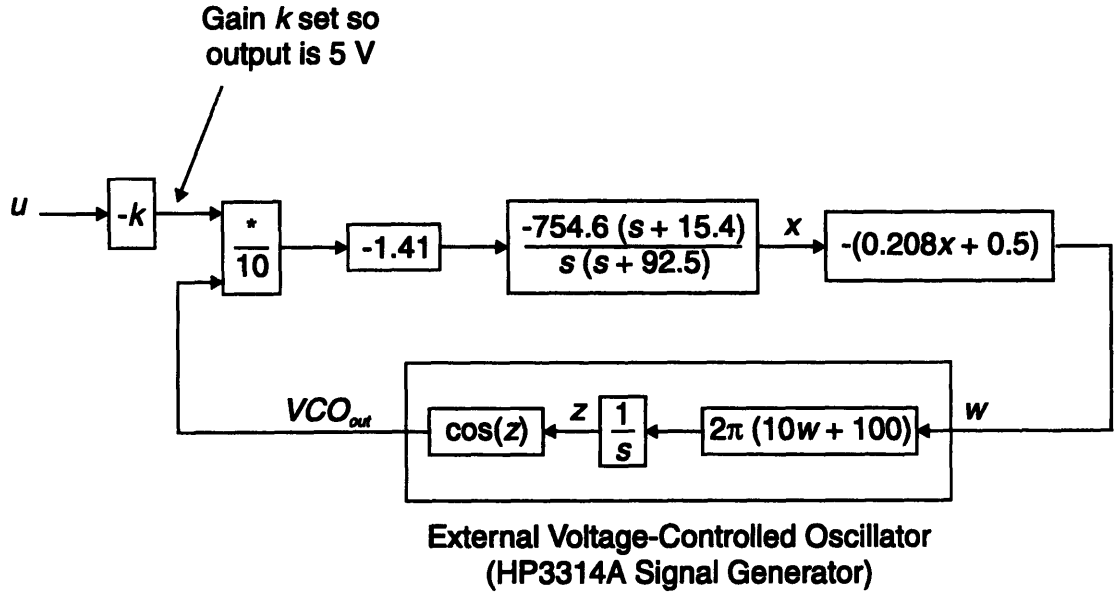

Figure 5-7: Phase-Lock Loop Block Diagram

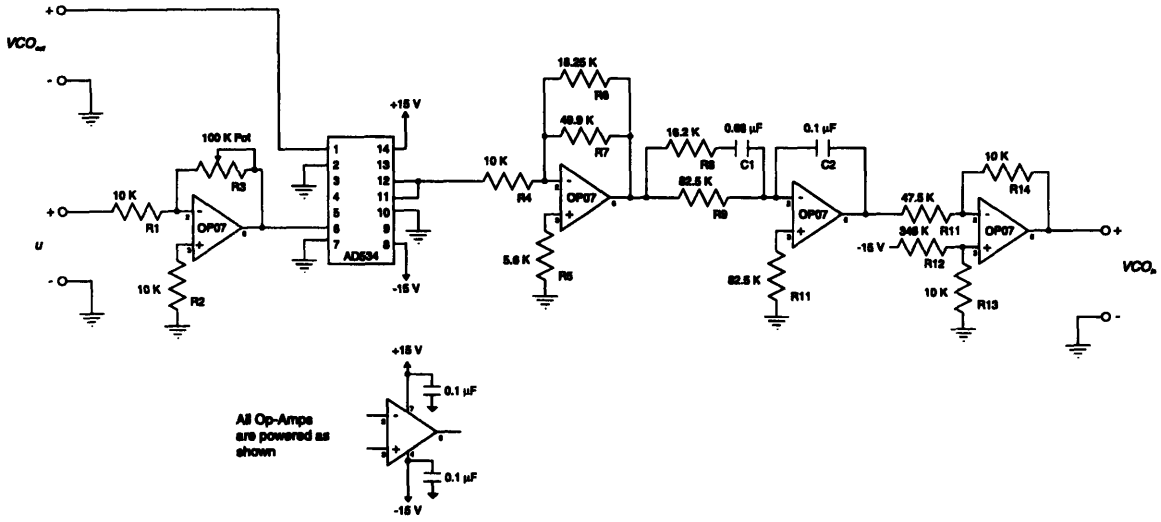

Figure 5-8: Phase-Lock Loop Schematic Diagram

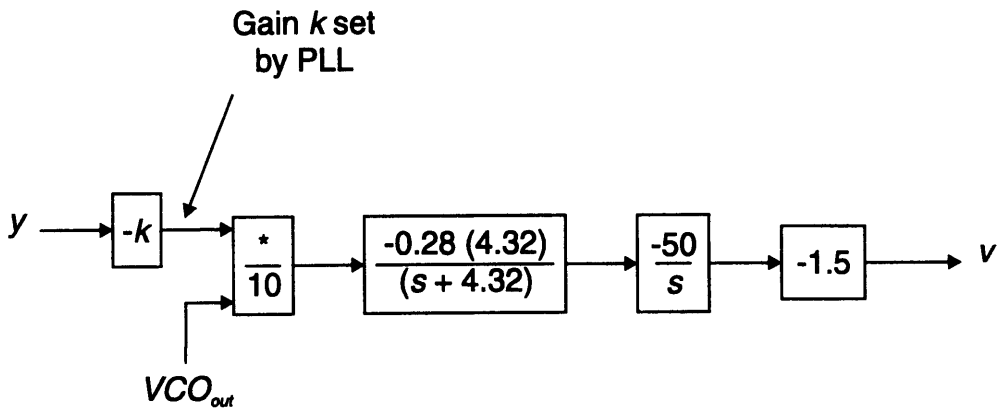

Figure 5-9: Frequency Control Loop Block Diagram

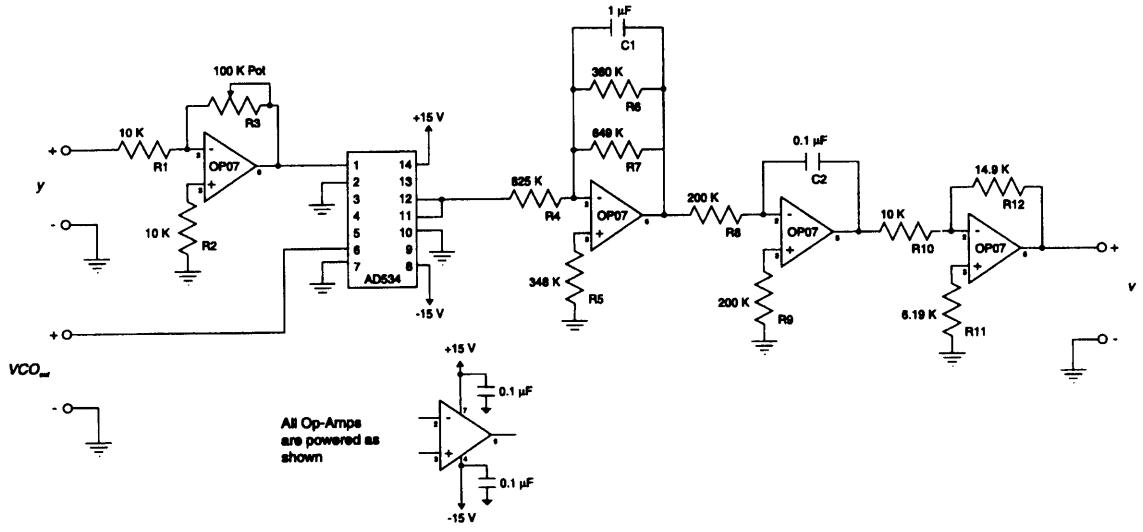

Figure 5-10: Frequency Control Loop Schematic Diagram

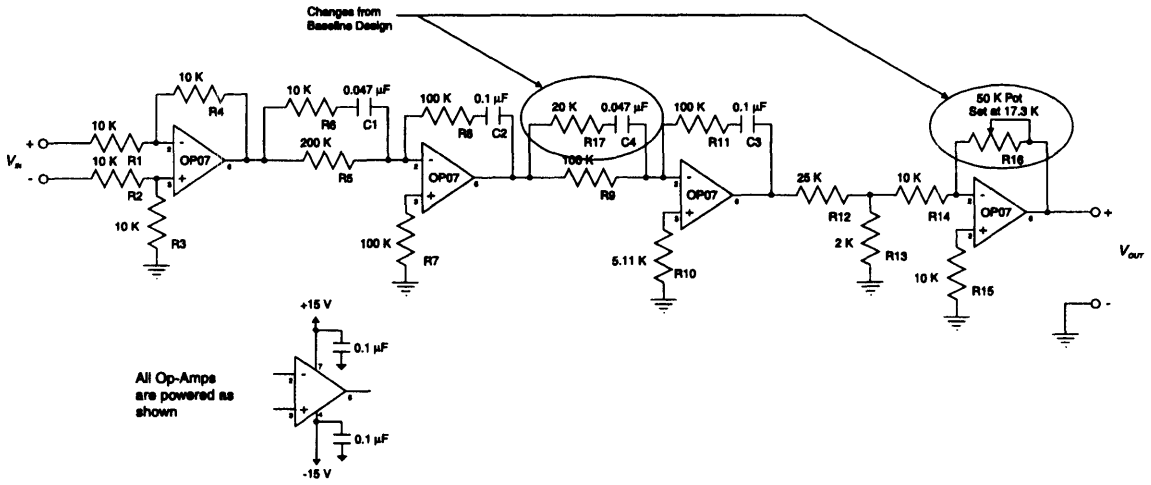

Figure 5-11: Notch Filter Controller

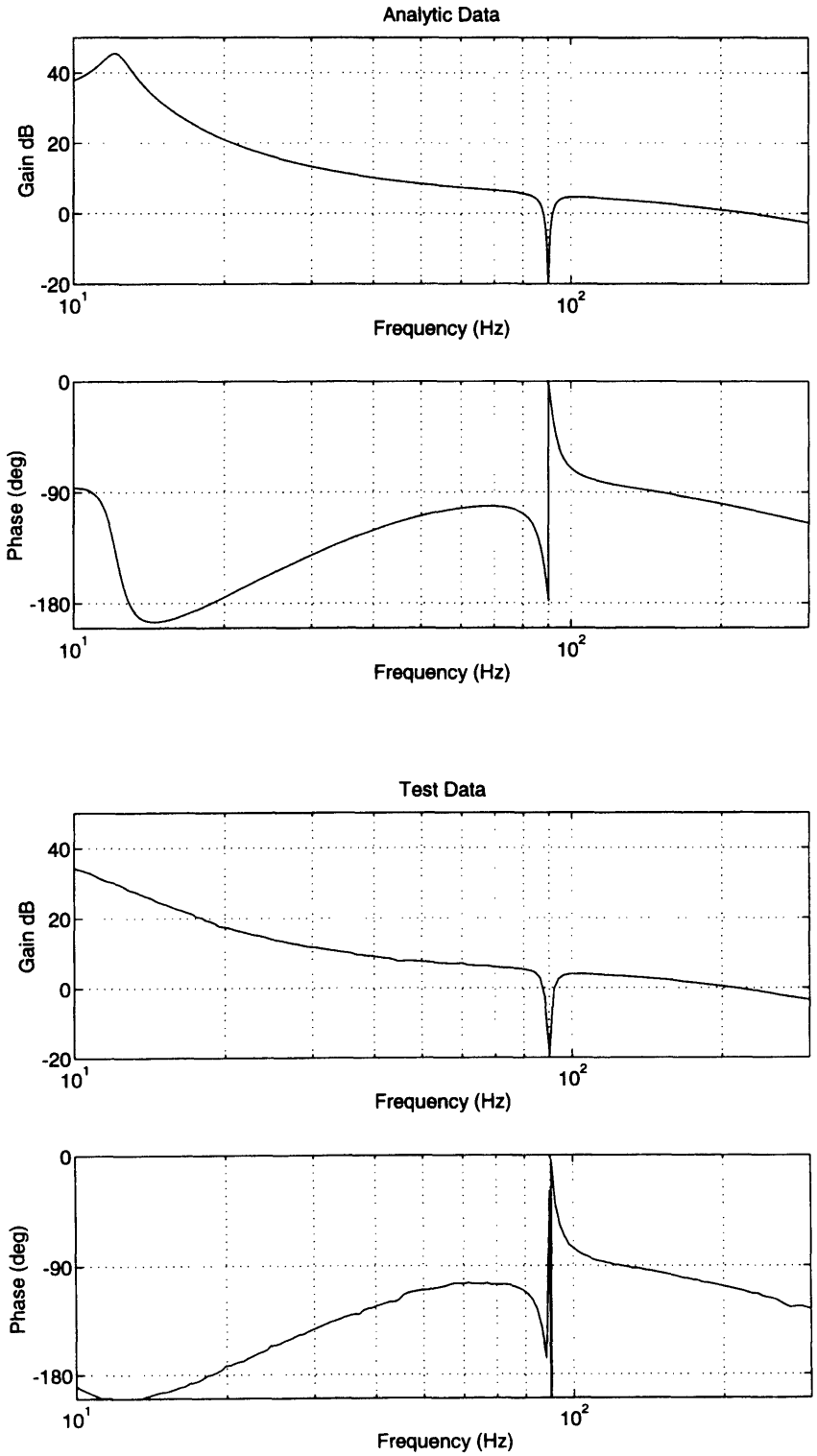

Figure 5-12: Notch Filter Design - Open-Loop Transfer Function

5.3 System Isolation and Base Jitter Disturbance Tests

The system isolation defines how well the mirror loop rejects base motion disturbance from the target pointing process and is defined as the transfer function from base motion, θ_{BI}, to the target receiver output, e_4, both measured as angles. The system isolation for the eliminator design is shown in Figure 5-13 and the system isolation for the notch filter design is shown in Figure 5-14. In both figures, the system isolation for the baseline design is shown as the dashed curve. For the eliminator design, there is some improvement in attenuation over the frequency band of 50 to 80 Hz; however, in the low-frequency band from 1 to 30 Hz, the attenuation is about 20 dB worse. For the notch filter design, the low-frequency attenuation is about the same as that for the baseline design and there is improved attenuation in the frequency band from 20 to 80 Hz.

The effective jitter stabilization bandwidth is defined to be the frequency range for which the system isolation is below -20 dB. The effective jitter stabilization bandwidth is approximately 35 Hz for the baseline design. For the eliminator design, the effective jitter stabilization bandwidth has decreased to 5 Hz which is primarily due to the low slope at crossover resulting in less attenuation around 10-20 Hz. On the other hand, the notch design has increased the effective jitter stabilization bandwidth to 50 Hz.

The base jitter disturbance test quantified the system isolation in terms of a specific jitter disturbance spectrum. The jitter spectrum of Figure 5-15 was applied to the base (test table). Figure 5-16 shows the target receiver output spectrum using the baseline controller. The baseline design has a total noise of 3.39 μrad r.m.s. over the frequency range of 0.125-100 Hz.

The spectrum for the eliminator design is shown in Figure 5-17. The effect of the reduced low-frequency attenuation becomes apparent in this test. The total noise over 0.125-100 Hz has increased to 24.83 μrad r.m.s., and of this total, 24.59 μrad r.m.s. is contained in the frequency band of 2 to 50 Hz.

The spectrum for the notch design is shown in Figure 5-18. The total noise over 0.125-100 Hz is 4.78 μrad r.m.s. This noise total is greater than that of the baseline design and most of this increase is contained in the frequency band of 85 to 95 Hz where the noise is 3.07 μrad r.m.s. It is expected that the noise at 90 Hz would be transferred to the receiver output. Because of the notch at 90 Hz within the mirror loop, the mirror will not be driven at this frequency and therefore the jitter disturbance at this frequency will be completely transferred to the

target receiver. Also, wideband jitter on the ORG beam is more highly coupled to the target receiver with the wide bandwidth mirror loop.

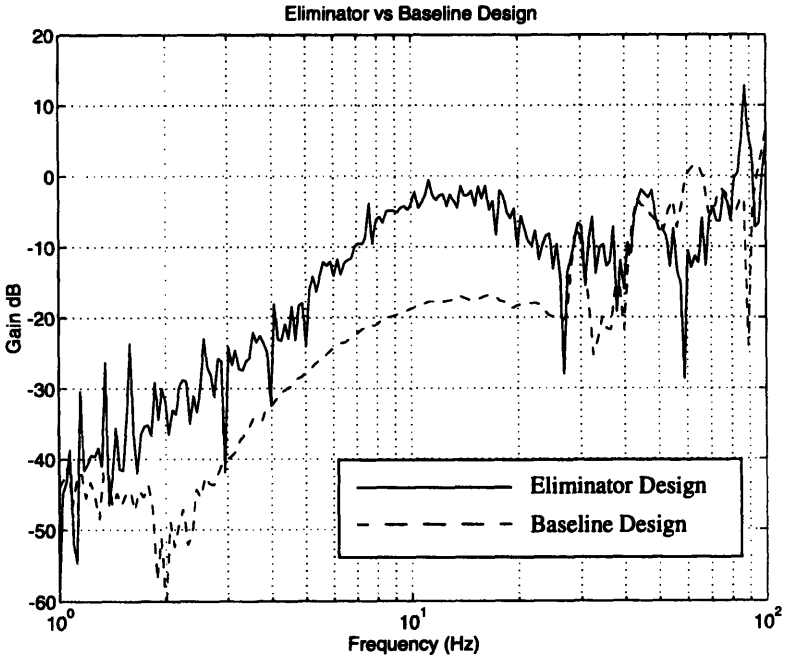

Figure 5-13: System Isolation for Eliminator Design

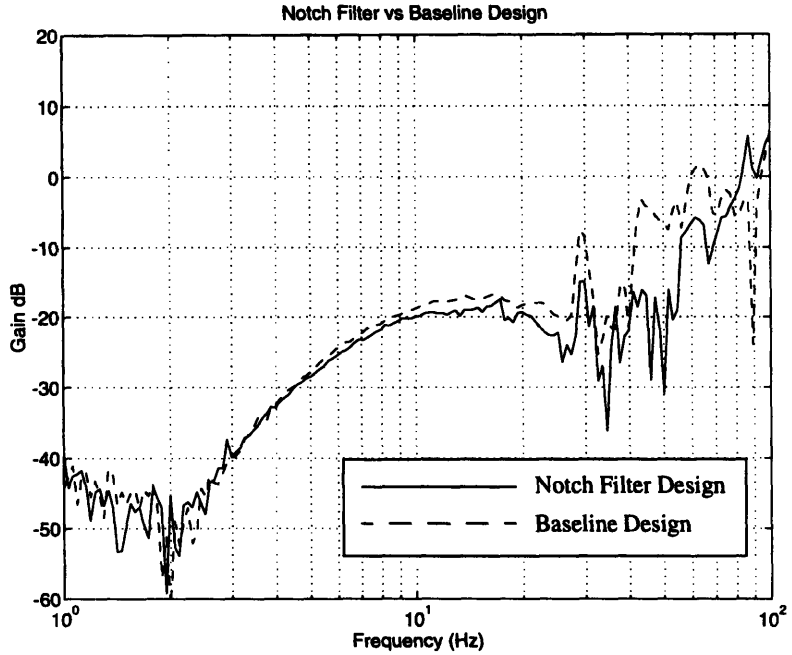

Figure 5-14: System Isolation for Notch Filter Design

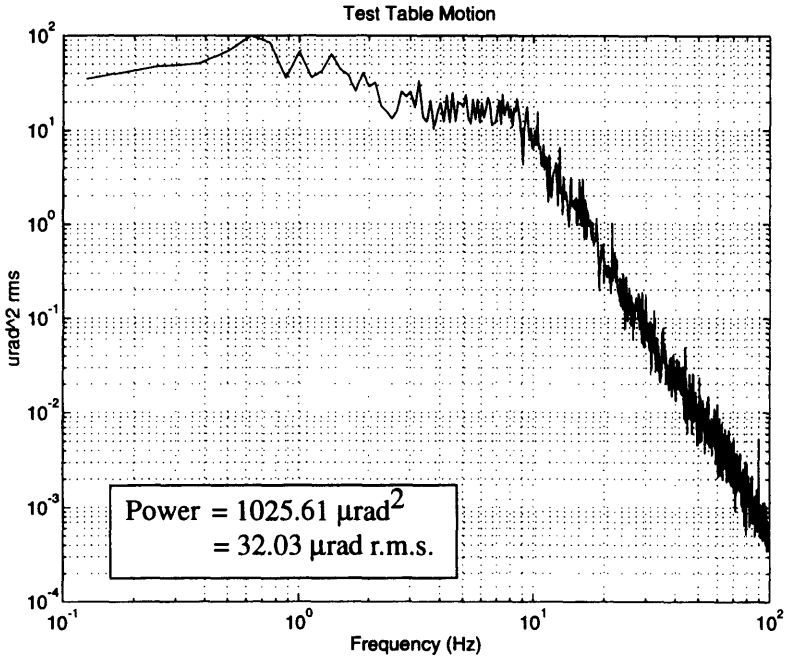

Figure 5-15: Power Spectrum of Test Table Jitter Disturbance

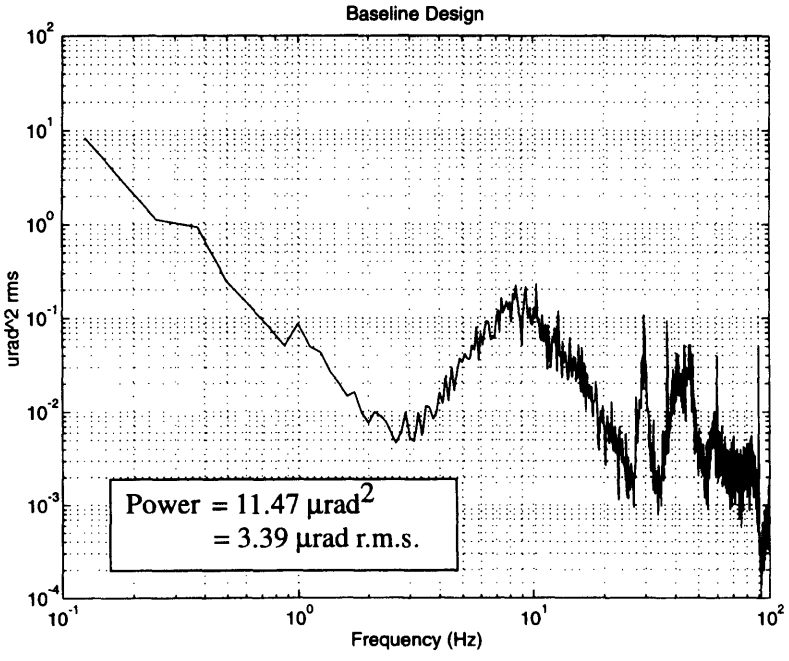

Figure 5-16: Power Spectrum of Target Receiver - Baseline Design

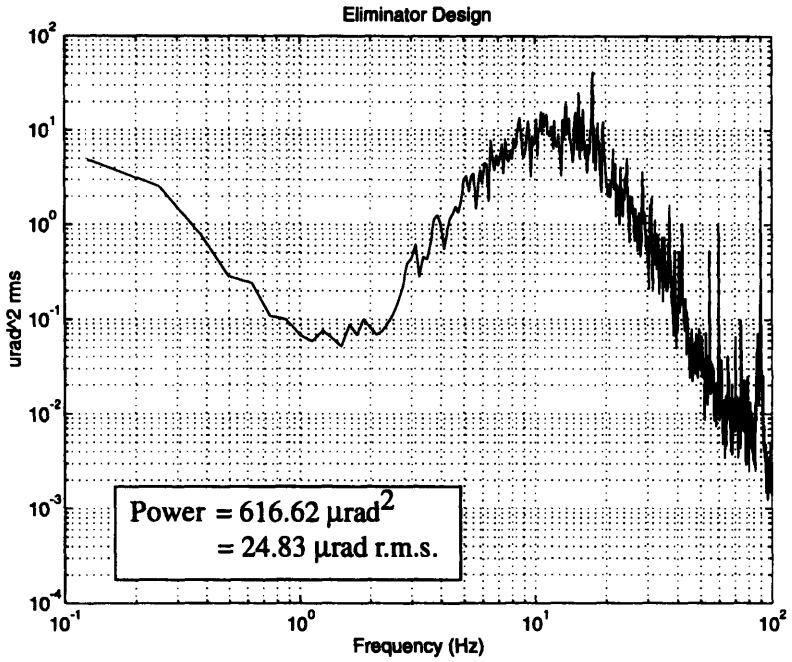

Figure 5-17: Power Spectrum of Target Receiver - Eliminator Design

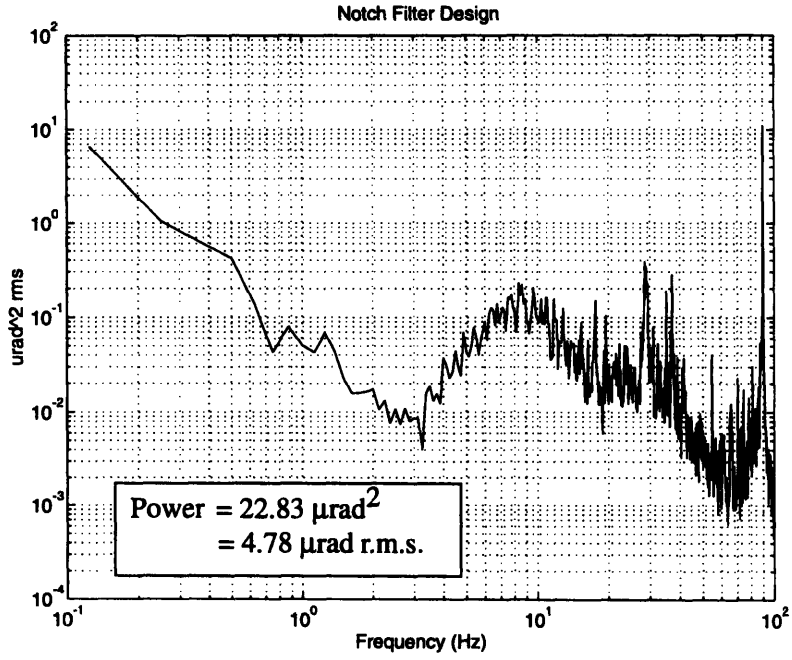

Figure 5-18: Power Spectrum of Target Receiver - Notch Filter Design

5.4 Results and Comparisons

From the hardware test results, the following are observed.

The primary disadvantage of the eliminator design is that, for higher bandwidths, the system isolation is substantially worse in the low-frequency region when compared to the notch filter design with an identical bandwidth. This is summarized by the effective jitter stabilization bandwidth which for the eliminator design is only 5 Hz compared to the 50 Hz bandwidth for the notch filter design (both designs with an open-loop crossover frequency of about 200 Hz).

The hardware test with the eliminator and a 240 Hz open-loop crossover also uncovered a low-frequency response within the mirror loop which was most apparent in the quad detector output. A power spectrum of the quad output showed this noise response was concentrated in the frequency band of 5 to 40 Hz. This noise response is due to the poor low-frequency disturbance rejection of the eliminator design. The frequency band of the low-frequency noise response corresponds to the hump in the system isolation transfer function of Figure 5-13. This figure also depicts the sensitivity function of the mirror loop and therefore, what is being seen is the transfer of the ORG broadband jitter to the quad detector output.

For these reasons, the eliminator design does not offer much benefit in extending the open-loop crossover frequency beyond the notch frequency.

The notch filter design, however, offers very good performance at higher bandwidths. Given a 200 Hz crossover frequency, the notch filter design does not degrade low-frequency attenuation of base disturbance and offers improved attenuation from 20-80 Hz when compared to the baseline design. But on the other hand, the notch filter design is sensitive to base disturbance around the notch frequency.

Two interesting phenomena were observed during these tests. First, the base jitter disturbance test showed that more noise is passed by the notch filter design (3.07 μrad r.m.s.) than the eliminator design(1.93 μrad r.m.s.) within the frequency band of 85 to 95 Hz. This may be an indication that the -3 dB frequency width of the notch filter is greater than for the eliminator thus passing more noise in the vicinity of the notch frequency.

The second phenomenon was that a 16 Hz discrete component was discovered on the quad detector output while investigating the low-frequency noise response. The ORG beam jitter contains additional high-frequency discrete components, two of which are at 540 Hz and 556 Hz. It is

believed that these two signals are mixing within the mirror loop. It does not appear that this mixing occurs within the eliminator as this phenomenon is apparent in the notch filter design as well. This discrete component disappears when a 540 Hz notch is placed in the mirror loop. The discrete component was not large enough to cause any significant performance degradation; however, this component grows as the open-loop gain at 540 Hz and 556 Hz increases. Thus, the amplitude of this discrete component is an increasing function of the mirror loop's crossover frequency.

As a final observation, it is noted that the benefit of extending the open-loop crossover frequency depends on the actual base disturbance spectrum. For the particular spectrum of the base jitter disturbance test, the increased bandwidth resulted in an increase in the target receiver noise for both the eliminator and notch filter designs.

Chapter 6: Conclusion and Recommendations

6.1 Conclusion

This thesis discussed methods for extending the open-loop crossover frequency of the pointing stabilization testbed's mirror loop. The mirror loop contains a notch-type filter to remove the ORG spin frequency discrete on the optical reference. Two "notch" filters were analyzed in this thesis, both with the ability to search for and lock onto the discrete disturbance. The *eliminator* electronically cancels the discrete by reconstructing the discrete through a phase-lock loop and an amplitude control loop, and nulls the discrete through feedback subtraction. A *tracking notch filter* was designed to duplicate the performance of the eliminator. The tracking notch filter is an ordinary linear notch filter with additional control circuitry to lock the notch frequency to the frequency of the discrete disturbance.

The common performance parameters of the eliminator and the tracking notch filter include, as a minimum, a 50 dB attenuation in the center of the notch, a 5 Hz -3 dB frequency width, and the ability to lock to a discrete signal in the frequency band of 80 to 100 Hz. The fundamental difference between the eliminator and the tracking notch filter is the amount of phase lag

induced at the notch frequency. The phase lag contributed by the eliminator is 180° while the tracking notch filter contributes 90° of phase lag.

It is possible to extend the open-loop crossover frequency beyond the notch frequency by adding lead compensation to the mirror loop. This thesis demonstrated a 200 Hz open-loop crossover for both the eliminator and tracking notch filter designs. For a given crossover frequency, the tracking notch filter design requires less lead compensation than the eliminator design. This results in better low-frequency disturbance rejection for the tracking notch filter design as compared to the eliminator design. The effective jitter stabilization bandwidth is 35 Hz for the baseline design, 5 Hz for the eliminator design, and 50 Hz for the notch filter design.

The tracking notch filter design has roughly the same level of low-frequency disturbance rejection and better rejection from 50-80 Hz when compared to the baseline design. Theoretically, by extending the crossover frequency even further, the overall performance of the notch filter can be improved. It is possible to extend the crossover frequency beyond 200 Hz but, as the crossover frequency increases, the ORG's higher frequency noise harmonics become more significant. These harmonics cause a low-frequency noise response in the mirror loop which increases in amplitude with increasing crossover frequency. Therefore, there is a trade-off between the mirror loop bandwidth and the effects of the ORG harmonics on system performance. This problem can be reduced by adding notch filters to attenuate the more significant ORG harmonics. Properly designed, these filters will have little effect on the mirror loop's open-loop transfer function at the spin frequency. There will come a point, however, that as the crossover frequency is increased, the phase of these notch filters will eventually affect the mirror loop's phase margin at the crossover frequency.

An improved ORG is currently under development. This ORG will have a spin frequency of 200 Hz. The techniques of this thesis can be applied to a system based on the improved ORG to achieve an open-loop crossover frequency of 450 Hz. The projected effective jitter stabilization bandwidth of this system is 110 Hz.

6.2 Recommendations for Future Research

The emphasis of this thesis was on proving that the open-loop crossover frequency of the mirror loop could be extended beyond the notch frequency. There still remains work to be done on optimizing the components of the mirror loop for a particular crossover frequency. Specifically, the notch filter design bears closer examination, especially the frequency width of the notch and the

bandwidths of the PLL and FCL. The trade-off between open-loop crossover frequency and the effects of higher-order ORG harmonics can be optimized once given the expected jitter disturbance spectrum for a specific application.

It is recommended that first the ORG spin frequency be increased as far as practical in order to increase the effective jitter stabilization bandwidth. Then the methods of this thesis can be used to extend the crossover frequency beyond the spin frequency.

As an alternative to the basic mirror loop design analyzed in this thesis, the eliminator function can be handled outside the mirror loop. This requires an additional quad detector and a separate loop to remove the discrete components from the ORG reference beam. It is recommended that the discrete noise be removed by directly torquing the gyro itself. The stability of the mirror loop will no longer be dependent on the ORG's discrete noise. Also, by directly torquing the gyro, it may be possible to remove the higher-order discrete harmonics of the spin frequency.

Appendix A: Modeling of the Subtraction Eliminator

The objective of this Appendix is to obtain a linear time-invariant (LTI) model for the subtraction eliminator. To achieve this, two intermediate models will be developed. The first intermediate model consists of a set of nonlinear differential equations taken directly from the eliminator block diagram. The second intermediate model is formed by linearizing the differential equations based on the assumption that the eliminator is in-lock. This results in a linear time-varying (LTV) model. The LTI eliminator model is formed from the LTV model by solving the LTV system for an arbitrary, periodic input. By varying the frequency of the input, a time-invariant transfer function is obtained. This transfer function becomes the LTI eliminator model.

A.1 The Nonlinear Eliminator Model

A set of nonlinear equations is obtained from the block diagram of the subtraction eliminator shown in Figure A-1. The nonlinear eliminator model is composed of seven differential equations defining the state of the system and a single output equation. These equations are

$$\dot{x}_1 = -k_1 x_1 + k_1 [k_{10} u - k_9 k_{10} x_6 \sin x_3 - x_7] \cos x_3 \quad \text{(A-1)}$$

$$\dot{x}_2 = k_2 x_1 + k_3 [k_{10} u - k_9 k_{10} x_6 \sin x_3 - x_7] \cos x_3 \quad \text{(A-2)}$$

$$\dot{x}_3 = k_4 x_2 + k_5 \quad \text{(A-3)}$$

$$\dot{x}_4 = -k_6 x_4 + k_6 [k_{10} u - k_9 k_{10} x_6 \sin x_3 - x_7] \sin x_3 \quad \text{(A-4)}$$

$$\dot{x}_5 = k_7 x_4 + k_8 [k_{10} u - k_9 k_{10} x_6 \sin x_3 - x_7] \sin x_3 \quad \text{(A-5)}$$

$$\dot{x}_6 = x_5 \quad \text{(A-6)}$$

$$\dot{x}_7 = k_{11} [k_{10} u - k_9 k_{10} x_6 \sin x_3 - x_7] \quad \text{(A-7)}$$

$$y = u - k_9 x_6 \sin x_3 \quad \text{(A-8)}$$

where x_1-x_7 and k_1-k_{11} are defined in Figure A-1.

A.2 The Linear Time-Varying (LTV) Eliminator Model

The LTV model is developed by linearizing the nonlinear differential equations. Assume that the eliminator is in-lock and that the nominal input is the locking signal given by

$$u_N(t) = A_0 \sin(\omega_0 t) \quad \text{(A-9)}$$

where for the ORG

$$A_0 = 0.9 \text{ V}$$
$$\omega_0 = 2\pi (90 \text{ Hz}) = 565.5 \text{ rad/sec}$$

With no other input, the nominal state trajectory corresponding to this input is

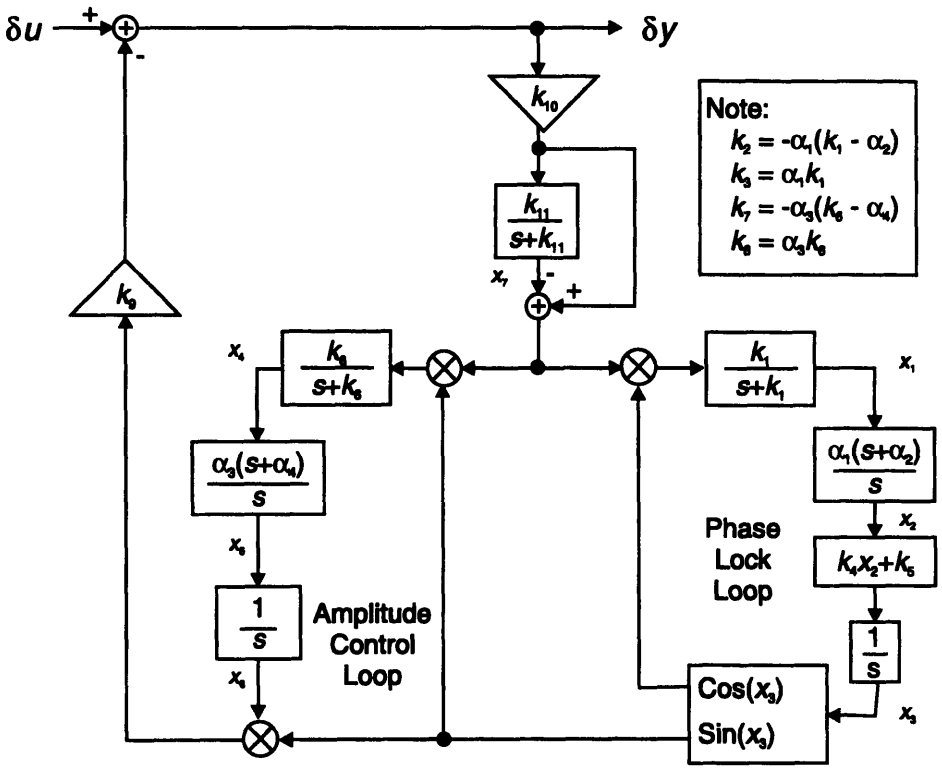

Figure A-1: Parametric Representation of the Subtraction Eliminator

$$x_N(t) = \begin{bmatrix} 0 \\ (\omega_0 - k_5)/k_4 \\ \omega_0 t \\ 0 \\ 0 \\ A_o/k_9 \\ 0 \end{bmatrix} \tag{A-10}$$

resulting in the nominal output

$$y_N(t) = 0 \tag{A-11}$$

Linearizing (A-1) -(A-8) about the nominal control and state trajectory given in (A-9) and (A-10) respectively yields the LTV perturbation model

$$\delta\dot{x}(t) = A(t)\,\delta x(t) + B(t)\,\delta u(t) \tag{A-12}$$

$$\delta y(t) = C(t)\,\delta x(t) + D\delta u(t) \tag{A-13}$$

where δu(t) is the control perturbation, δx(t) is the state perturbation, and δy(t) is the output perturbation. The matrices *A(t)*, *B(t)*, *C(t)*, and *D* are given by

$$A(t) = \begin{bmatrix} -k_1 & 0 & -k_1k_{10}A_0\cos^2(\omega_0 t) & 0 & 0 & -k_1k_9k_{10}\sin(\omega_0 t)\cos(\omega_0 t) & -k_1\cos(\omega_0 t) \\ k_2 & 0 & -k_3k_{10}A_0\cos^2(\omega_0 t) & 0 & 0 & -k_3k_9k_{10}\sin(\omega_0 t)\cos(\omega_0 t) & -k_3\cos(\omega_0 t) \\ 0 & k_4 & 0 & 0 & 0 & 0 & 0 \\ 0 & 0 & -k_6k_{10}A_0\sin(\omega_0 t)\cos(\omega_0 t) & -k_6 & 0 & -k_6k_9k_{10}\sin^2(\omega_0 t) & -k_6\sin(\omega_0 t) \\ 0 & 0 & -k_8k_{10}A_0\sin(\omega_0 t)\cos(\omega_0 t) & k_7 & 0 & -k_8k_9k_{10}\sin^2(\omega_0 t) & -k_8\sin(\omega_0 t) \\ 0 & 0 & 0 & 0 & 1 & 0 & 0 \\ 0 & 0 & -k_{10}k_{11}A_0\cos(\omega_0 t) & 0 & 0 & -k_9k_{10}k_{11}\sin(\omega_0 t) & -k_{11} \end{bmatrix}$$

$$B(t) = \begin{bmatrix} k_1k_{10}\cos(\omega_0 t) \\ k_3k_{10}\cos(\omega_0 t) \\ 0 \\ k_6k_{10}\sin(\omega_0 t) \\ k_8k_{10}\sin(\omega_0 t) \\ 0 \\ k_{10}k_{11} \end{bmatrix}$$

$$C(t) = \begin{bmatrix} 0 & 0 & -A_0\cos(\omega_0 t) & 0 & 0 & -k_9\sin(\omega_0 t) & 0 \end{bmatrix}$$

$$D = 1$$

The total control, states, and output trajectories are a sum of the nominal and perturbed values

$$u(t) = u_N(t) + \delta u(t) \tag{A-14}$$

$$x(t) = x_N(t) + \delta x(t) \tag{A-15}$$

$$\begin{aligned} y(t) &= y_N(t) + \delta y(t) \\ &= \delta y(t) \end{aligned} \tag{A-16}$$

A.3 The Linear Time-Invariant (LTI) Eliminator Model

It is assumed that the eliminator is in-lock and that the locking signal $u_N(t)$ can be absorbed into the LTI eliminator model. The LTI model will thus describe the input-output relationship for $\delta u(t)$ and $\delta y(t)$. (It is for this reason that $d(t)$ was shown as a direct input to the eliminator in Figure 2-3.)

The LTI eliminator model is formed in two steps:

1) Equations (A-12) and (A-13) are solved for $\delta y(t)$ given an arbitrary, periodic input $\delta u(t)$.

2) The relationship between $\delta u(t)$ and $\delta y(t)$ is then simplified to form a time-invariant transfer function.

A.3.1 Solution to the LTV Model

The LTV equations given by (A-12) and (A-13) can be rewritten as follows

$$\dot{x}_1 = -k_1 x_1 + k_1 \cos(\omega_0 t)\ (k_{10}\delta y - x_7) \tag{A-17}$$

$$\dot{x}_2 = k_2 x_1 + k_3 \cos(\omega_0 t)\ (k_{10}\delta y - x_7) \tag{A-18}$$

$$\dot{x}_3 = k_4 x_2 \tag{A-19}$$

$$\dot{x}_4 = -k_6 x_4 + k_6 \sin(\omega_0 t)\ (k_{10}\delta y - x_7) \tag{A-20}$$

$$\dot{x}_5 = k_7 x_4 + k_8 \sin(\omega_0 t)\ (k_{10}\delta y - x_7) \tag{A-21}$$

$$\dot{x}_6 = x_5 \tag{A-22}$$

$$\dot{x}_7 = k_{11}(k_{10}\delta y - x_7) \tag{A-23}$$

$$\delta y = \delta u - A_0 \cos(\omega_0 t)\, x_3 - k_9 \sin(\omega_0 t)\, x_6 \tag{A-24}$$

To solve for $\delta y(t)$, the forms of x_3, x_6 and x_7 will be assumed. Then, these variables will be propagated through equations (A-17)-(A-23) to construct a new form x_3', x_6', and x_7'. These two forms will be shown to be equivalent and, by equating them, the constants that define the original form can be solved.

Let the perturbed input be a complex exponential of arbitrary frequency ω

$$\delta u(t) = e^{j\omega t} \tag{A-25}$$

Assume that the solutions to x_3, x_6, and x_7 take on the following form

$$x_3 = \sum_{n=-\infty}^{\infty} a_n e^{j(\omega - n\omega_0)t}, \qquad n = \text{odd} \tag{A-26}$$

$$x_6 = \sum_{n=-\infty}^{\infty} b_n e^{j(\omega - n\omega_0)t}, \qquad n = \text{odd} \tag{A-27}$$

$$x_7 = \sum_{n=-\infty}^{\infty} c_n e^{j(\omega - n\omega_0)t}, \qquad n = \text{even} \tag{A-28}$$

Define the variable v_1 to be

$$v_1 \equiv k_{10}\delta y - x_7 \tag{A-29}$$

Substituting the complex exponential identity for sine and cosine along with (A-24) and (A-25)-(A-28) into (A-29) and performing some algebraic simplification yields

$$v_1 = \sum_{n=-\infty}^{\infty} d_n e^{j(\omega - n\omega_0)t}, \qquad n = \text{even} \tag{A-30}$$

where

$$\begin{aligned} d_n &= \frac{1}{2}k_{10}\left(-A_0\left(a_{n+1} + a_{n-1}\right) + jk_9\left(b_{n+1} - b_{n-1}\right)\right) - c_n, \qquad n = \text{even},\ n \neq 0 \\ d_0 &= \frac{1}{2}k_{10}\left(-A_0\left(a_1 + a_{-1}\right) + jk_9\left(b_1 - b_{-1}\right)\right) - c_0 + k_{10} \end{aligned} \tag{A-31}$$

Substituting (A-30) into (A-23) and integrating to solve for x_7 produces

$$x_7 = \sum_{n=-\infty}^{\infty} \frac{k_{11} d_n}{j(\omega - n\omega_0)} e^{j(\omega - n\omega_0)t}, \qquad n = \text{even} \tag{A-32}$$

Equating (A-28) and (A-32) yields

$$c_n = \frac{k_{11} d_n}{j(\omega - n\omega_0)}, \qquad n = \text{even} \tag{A-33}$$

The constants c_n expressed in terms of a_n and b_n are obtained by substituting (A-31) into (A-33) and solving for c_n:

$$c_n = \frac{\frac{1}{2}k_{10}k_{11}}{k_{11}+j(\omega-n\omega_0)}\left[-A_0(a_{n+1}+a_{n-1})+jk_9(b_{n+1}-b_{n-1})\right]$$

$$n = \text{even},\ n \neq 0 \qquad \text{(A-34)}$$

$$c_0 = \frac{\frac{1}{2}k_{10}k_{11}}{k_{11}+j\omega}\left[-A_0(a_1+a_{-1})+jk_9(b_1-b_{-1})\right]+\frac{k_{10}k_{11}}{k_{11}+j\omega}$$

The next step is to propagate (A-30) through (A-17)-(A-19). First, define

$$\begin{aligned} v_2 &\equiv \cos(\omega_0 t)\, v_1 \\ &= \sum_{n=-\infty}^{\infty} \frac{1}{2}(d_{n+1}+d_{n-1})\, e^{j(\omega-n\omega_0)t}, \qquad n = \text{odd} \end{aligned} \qquad \text{(A-35)}$$

and assume x_1 has the following form

$$x_1 = \sum_{n=-\infty}^{\infty} e_n e^{j(\omega-n\omega_0)t}, \qquad n = \text{odd} \qquad \text{(A-36)}$$

Substituting (A-35) and (A-36) into (A-17) produces

$$\dot{x}_1 = \sum_{n=-\infty}^{\infty} k_1\left(-e_n+\frac{1}{2}(d_{n+1}+d_{n-1})\right)e^{j(\omega-n\omega_0)t}, \qquad n = \text{odd} \qquad \text{(A-37)}$$

Differentiating (A-36) and equating it to (A-37) yields

$$e_n = \frac{\frac{1}{2}k_1}{k_1+j(\omega-n\omega_0)}(d_{n+1}+d_{n-1}), \qquad n = \text{odd} \qquad \text{(A-38)}$$

Substituting (A-35) and (A-36) into (A-18) and integrating to solve for x_2 gives

$$x_2 = \sum_{n=-\infty}^{\infty} \frac{1}{j(\omega-n\omega_0)}\left(k_2 e_n+\frac{1}{2}k_3(d_{n+1}+d_{n-1})\right)e^{j(\omega-n\omega_0)t}, \qquad n = \text{odd} \qquad \text{(A-39)}$$

(Assuming that the constant of integration is zero which will be the case when the eliminator is in-lock).

Equations (A-19) and (A-39) are combined and then integrated to produce

$$x_3 = -\sum_{n=-\infty}^{\infty} \frac{k_4}{(\omega - n\omega_0)^2}\left(k_2 e_n + \frac{1}{2} k_3 (d_{n+1} + d_{n-1}) \right) e^{j(\omega - n\omega_0)t}, \qquad n = \text{odd} \tag{A-40}$$

(Again, ignoring the constant of integration.)

Equating (A-40) with (A-26) yields

$$a_n = -\frac{k_4}{(\omega - n\omega_0)^2}\left(k_2 e_n + \frac{1}{2} k_3 (d_{n+1} + d_{n-1}) \right), \qquad n = \text{odd} \tag{A-41}$$

Through a similar derivation of propagating (A-30) through (A-20)-(A-22), the following results are obtained:

$$x_4 = \sum_{n=-\infty}^{\infty} f_n e^{j(\omega - n\omega_0)t}, \qquad n = \text{odd} \tag{A-42}$$

$$f_n = \frac{-j\frac{1}{2}k_6}{k_6 + j(\omega - n\omega_0)} (d_{n+1} - d_{n-1}), \qquad n = \text{odd} \tag{A-43}$$

$$b_n = -\frac{1}{(\omega - n\omega_0)^2}\left(k_7 f_n - j\frac{1}{2} k_8 (d_{n+1} - d_{n-1}) \right), \qquad n = \text{odd} \tag{A-44}$$

The following definitions will be used to simplify the solution to a_n and b_n:

$$\alpha_1(n) \equiv \frac{-j\frac{1}{2}k_{10}A_0(\omega - n\omega_0)}{k_{11} + j(\omega - n\omega_0)}, \qquad n = \text{even} \tag{A-45}$$

$$\alpha_2(n) \equiv \frac{-\frac{1}{2}k_9 k_{10}(\omega - n\omega_0)}{k_{11} + j(\omega - n\omega_0)}, \qquad n = \text{even} \tag{A-46}$$

$$\alpha_3(n) \equiv \begin{cases} \dfrac{jk_{10}\omega}{k_{11} + j\omega}, & n = 0 \\ 0 & \text{otherwise} \end{cases} \tag{A-47}$$

$$\alpha_4(n) \equiv \frac{-\frac{1}{2}k_4}{(\omega - n\omega_0)^2}\left(\frac{k_1 k_2}{k_1 + j(\omega - n\omega_0)} + k_3 \right), \qquad n = \text{odd} \tag{A-48}$$

$$\alpha_5(n) \equiv \frac{j\frac{1}{2}}{(\omega - n\omega_0)^2}\left(\frac{k_6 k_7}{k_6 + j(\omega - n\omega_0)} + k_8 \right), \qquad n = \text{odd} \tag{A-49}$$

Using these definitions, (A-33), (A-34), (A-38), (A-41), (A-43) and (A-44) can be summarized into three equations:

$$d_n = \alpha_1(n)\,(a_{n+1} + a_{n-1}) + \alpha_2(n)\,(b_{n+1} - b_{n-1}) + \alpha_3(n) \tag{A-50}$$

$$a_n = \alpha_4(n)\,(d_{n+1} + d_{n-1}) \tag{A-51}$$

$$b_n = \alpha_5(n)\,(d_{n+1} - d_{n-1}) \tag{A-52}$$

Substituting (A-50) into (A-51) and (A-52) yields

$$\begin{aligned}
&[\alpha_1(n+1)\,\alpha_4(n)]\,a_{n+2} + [(\alpha_1(n+1) + \alpha_1(n-1))\,\alpha_4(n) - 1]\,a_n + \\
&\quad [\alpha_1(n-1)\,\alpha_4(n)]\,a_{n-2} + [\alpha_2(n+1)\,\alpha_4(n)]\,b_{n+2} + \\
&\quad [(\alpha_2(n-1) - \alpha_2(n+1))\,\alpha_4(n)]\,b_n + [-\alpha_2(n-1)\,\alpha_4(n)]\,b_{n-2} + \\
&\quad [(\alpha_3(n+1) + \alpha_3(n-1))\,\alpha_4(n)] = 0
\end{aligned} \tag{A-53}$$

$$\begin{aligned}
&[\alpha_1(n+1)\,\alpha_5(n)]\,a_{n+2} + [(\alpha_1(n+1) - \alpha_1(n-1))\,\alpha_5(n)]\,a_n + \\
&\quad [-\alpha_1(n-1)\,\alpha_5(n)]\,a_{n-2} + [\alpha_2(n+1)\,\alpha_5(n)]\,b_{n+2} + \\
&\quad [-(\alpha_2(n+1) + \alpha_2(n-1))\,\alpha_5(n) - 1]\,b_n + [\alpha_2(n-1)\,\alpha_5(n)]\,b_{n-2} + \\
&\quad [(\alpha_3(n+1) - \alpha_3(n-1))\,\alpha_5(n)] = 0
\end{aligned} \tag{A-54}$$

For an arbitrary odd positive integer M, assume that

$$a_n = b_n = 0, \qquad |n| > M$$

Then the constants a_n and b_n can be solved via the following $(2M+2)\times(2M+2)$ matrix equation:

$$
\begin{pmatrix}
\beta_2(-M) & \beta_1(-M) & 0 & \dots & 0 & 0 & 0 \\
\beta_3(-M+2) & \beta_2(-M+2) & \beta_1(-M+2) & \dots & 0 & 0 & 0 \\
0 & \beta_3(-M+4) & \beta_2(-M+4) & \dots & 0 & 0 & 0 \\
\vdots & \vdots & \vdots & & \vdots & \vdots & \vdots \\
0 & 0 & 0 & \dots & \beta_2(M-4) & \beta_1(M-4) & 0 \\
0 & 0 & 0 & \dots & \beta_3(M-2) & \beta_2(M-2) & \beta_1(M-2) \\
0 & 0 & 0 & \dots & 0 & \beta_3(M) & \beta_2(M)
\end{pmatrix}
$$

$$
\begin{pmatrix}
\gamma_2(-M) & \gamma_1(-M) & 0 & \dots & 0 & 0 & 0 \\
\gamma_3(-M+2) & \gamma_2(-M+2) & \gamma_1(-M+2) & \dots & 0 & 0 & 0 \\
0 & \gamma_3(-M+4) & \gamma_2(-M+4) & \dots & 0 & 0 & 0 \\
\vdots & \vdots & \vdots & & \vdots & \vdots & \vdots \\
0 & 0 & 0 & \dots & \gamma_2(M-4) & \gamma_1(M-4) & 0 \\
0 & 0 & 0 & \dots & \gamma_3(M-2) & \gamma_2(M-2) & \gamma_1(M-2) \\
0 & 0 & 0 & \dots & 0 & \gamma_3(M) & \gamma_2(M)
\end{pmatrix}
$$

$$
\begin{bmatrix}
\beta_5(-M) & \beta_4(-M) & 0 & \dots & 0 & 0 & 0 \\
\beta_6(-M+2) & \beta_5(-M+2) & \beta_4(-M+2) & \dots & 0 & 0 & 0 \\
0 & \beta_6(-M+4) & \beta_5(-M+4) & \dots & 0 & 0 & 0 \\
\vdots & \vdots & \vdots & & \vdots & \vdots & \vdots \\
0 & 0 & 0 & \dots & \beta_5(M-4) & \beta_4(M-4) & 0 \\
0 & 0 & 0 & \dots & \beta_6(M-2) & \beta_5(M-2) & \beta_4(M-2) \\
0 & 0 & 0 & \dots & 0 & \beta_6(M) & \beta_5(M)
\end{bmatrix}
\times
$$

$$
\begin{bmatrix}
\gamma_5(-M) & \gamma_4(-M) & 0 & \dots & 0 & 0 & 0 \\
\gamma_6(-M+2) & \gamma_5(-M+2) & \gamma_4(-M+2) & \dots & 0 & 0 & 0 \\
0 & \gamma_6(-M+4) & \gamma_5(-M+4) & \dots & 0 & 0 & 0 \\
\vdots & \vdots & \vdots & & \vdots & \vdots & \vdots \\
0 & 0 & 0 & \dots & \gamma_5(M-4) & \gamma_4(M-4) & 0 \\
0 & 0 & 0 & \dots & \gamma_6(M-2) & \gamma_5(M-2) & \gamma_4(M-2) \\
0 & 0 & 0 & \dots & 0 & \gamma_6(M) & \gamma_5(M)
\end{bmatrix}
$$

$$\begin{bmatrix} a_{-M} \\ a_{-M+2} \\ a_{-M+4} \\ \vdots \\ a_{M-4} \\ a_{M-2} \\ a_{M} \\ \\ b_{-M} \\ b_{-M+2} \\ b_{-M+4} \\ \vdots \\ b_{M-4} \\ b_{M-2} \\ b_{M} \end{bmatrix} = - \begin{bmatrix} \beta_7(-M) \\ \beta_7(-M+2) \\ \beta_7(-M+4) \\ \vdots \\ \beta_7(M-4) \\ \beta_7(M-2) \\ \beta_7(M) \\ \\ \gamma_7(-M) \\ \gamma_7(-M+2) \\ \gamma_7(-M+4) \\ \vdots \\ \gamma_7(M-4) \\ \gamma_7(M-2) \\ \gamma_7(M) \end{bmatrix} \tag{A-55}$$

where β and γ are defined as follows for n=odd.

$$\beta_1(n) \equiv \alpha_1(n+1)\,\alpha_4(n)$$

$$\beta_2(n) \equiv (\alpha_1(n+1) + \alpha_1(n-1))\,\alpha_4(n) - 1$$

$$\beta_3(n) \equiv \alpha_1(n-1)\,\alpha_4(n)$$

$$\beta_4(n) \equiv \alpha_2(n+1)\,\alpha_4(n)$$

$$\beta_5(n) \equiv (\alpha_2(n-1) - \alpha_2(n+1))\,\alpha_4(n)$$

$$\beta_6(n) \equiv -\alpha_2(n-1)\,\alpha_4(n)$$

$$\beta_7(n) \equiv (\alpha_3(n+1) + \alpha_3(n-1))\,\alpha_4(n)$$

$$\gamma_1(n) \equiv \alpha_1(n+1)\,\alpha_5(n)$$

$$\gamma_2(n) \equiv (\alpha_1(n+1) - \alpha_1(n-1))\,\alpha_5(n)$$

$$\gamma_3(n) \equiv -\alpha_1(n-1)\,\alpha_5(n)$$

$$\gamma_4(n) \equiv \alpha_2(n+1)\,\alpha_5(n)$$

$$\gamma_5(n) \equiv -(\alpha_2(n+1) + \alpha_2(n-1))\,\alpha_5(n) - 1$$

$$\gamma_6(n) \equiv \alpha_2(n-1)\,\alpha_5(n)$$

$$\gamma_7(n) \equiv (\alpha_3(n+1) - \alpha_3(n-1))\,\alpha_5(n)$$

The constants c_n and d_n can be solved from a_n and b_n using equations (A-31) and (A-33). From (A-28), (A-29) and (A-30), the output $\delta y(t)$ can be expressed as

$$\delta y = \sum_{n=-\infty}^{\infty} y_n e^{j(\omega - n\omega_0)t}, \qquad n = \text{even} \tag{A-56}$$

where

$$y_n = \left(\frac{c_n + d_n}{k_{10}}\right), \qquad n = \text{even} \tag{A-57}$$

A.3.2 Simplification of the LTV Solution

Given an input at frequency ω, the previous section showed that the output will have a primary harmonic component at the same frequency ω plus additional harmonics at frequencies ω-$n\omega_0$, for even n. Using the parameters for the subtraction eliminator [see (A-67) later], it was observed that the additional harmonic terms approached zero as $|n| \rightarrow \infty$, validating the approximation that a_n and b_n are zero for large $|n|$. In fact, the additional harmonic terms tend to be small for all $n \neq 0$. Analysis of the LTV model shows that the largest additional harmonic term occurs at $n = 2$. This harmonic becomes significant only around the "notch" frequency; nonetheless, the magnitude of the $n = 2$ harmonic never exceeds -10 dB and is always smaller than the primary $(n = 0)$ harmonic. To develop the LTI model, all harmonic terms, except the $n = 0$ term, are assumed to be zero.

Assume that $d_n = 0$ for all $n \neq 0$ and that $a_n = b_n = 0$ for all $n \neq -1, 1$. Also assume that the PLL and ACL low pass filters are identical so that $k_1 = k_6$. Then equations (A-50)-(A-52) become

$$d_0 = \alpha_1(0)\,(\alpha_1 + a_{-1}) + \alpha_2(0)\,(b_1 - b_{-1}) + \alpha_3(0) \tag{A-58}$$

$$a_1 = \alpha_4(1)\,d_0 \tag{A-59}$$

$$a_{-1} = \alpha_4(-1)\,d_0 \tag{A-60}$$

$$b_1 = -\alpha_5(1)\,d_0 \tag{A-61}$$

$$b_{-1} = \alpha_5(-1)\,d_0 \tag{A-62}$$

Combining (A-58)-(A-62) yields

$$d_0 = [\alpha_1(0)\,(\alpha_4(1) + \alpha_4(-1)) - \alpha_2(0)\,(\alpha_5(1) + \alpha_5(-1))]\,d_0 + \alpha_3(0) \tag{A-63}$$

or by solving for d_0,

$$d_0 = \frac{\alpha_3(0)}{1-\alpha_1(0)\,(\alpha_4(1)+\alpha_4(-1))+\alpha_2(0)\,(\alpha_5(1)+\alpha_5(-1))} \tag{A-64}$$

Combining (A-33), (A-57), and (A-64) produces

$$y_0 = \left(\frac{j\omega + k_{11}}{j\omega k_{10}}\right)\frac{\alpha_3(0)}{1-\alpha_1(0)\,(\alpha_4(1)+\alpha_4(-1))+\alpha_2(0)\,(\alpha_5(1)+\alpha_5(-1))} \tag{A-65}$$

Using (A-45)-(A-49) and defining $s = j\omega$, Equation (A-65) and much algebraic manipulation simplifies

$$y_0 = \frac{(s+k_{11})\,(s^2+2k_1 s+k_1^2+\omega_0^2)\,(s^2+\omega_0^2)^2}{s^7+n_6 s^6+n_5 s^5+n_4 s^4+n_3 s^3+n_2 s^2+n_1 s+n_0} \tag{A-66}$$

where

$$n_0 = \omega_0^6 k_{11} + k_1^2 k_{11}\omega_0^4$$

$$n_1 = \omega_0^6 + k_1^2\omega_0^4 + 2k_1 k_{11}\omega_0^4 - \frac{1}{2}k_{10}\omega_0^2\,(k_4 A_0\,(k_1^2\,(k_2+k_3)+k_3\omega_0^2)+k_9\,(k_1^2\,(k_7+k_8)+k_8\omega_0^2))$$

$$n_2 = 2k_1\omega_0^4 + 3k_{11}\omega_0^4 + 2k_1^2 k_{11}\omega_0^2 - \frac{1}{2}k_1 k_{10}\omega_0^2\,(k_4 A_0\,(3k_2+2k_3)+k_9\,(3k_7+2k_8))$$

$$n_3 = 3\omega_0^4 + 2k_1^2\omega_0^2 + 4k_1 k_{11}\omega_0^2 + \frac{1}{2}k_1^2 k_{10}\,(k_4 A_0\,(k_2+k_3)+k_9\,(k_7+k_8))$$

$$n_4 = 4k_1\omega_0^2 + 3k_{11}\omega_0^2 + k_1^2 k_{11} + \frac{1}{2}k_1 k_{10}\,(k_4 A_0\,(k_2+2k_3)+k_9\,(k_7+2k_8))$$

$$n_5 = 3\omega_0^2 + k_1^2 + 2k_1 k_{11} + \frac{1}{2}k_{10}\,(k_3 k_4 A_0 + k_8 k_9)$$

$$n_6 = 2k_1 + k_{11}$$

Since y_0 represents the output at frequency ω given a unit input at the same frequency, Equation (A-66) can be viewed as a transfer function between the input and the output of the eliminator. This forms the seventh-order LTI model for the eliminator.

The parameters for the subtraction eliminator as shown in Figure 2-5 are

$$\begin{array}{lll} k_1 = 100 & k_5 = 657.3 & k_9 = 0.22 \\ k_2 = -9 & k_6 = 100 & k_{10} = 5.56 \\ k_3 = 10 & k_7 = -5439.6 & k_{11} = 100 \\ k_4 = 89.85 & k_8 = 6044 & \end{array} \qquad \text{(A-67)}$$

Substituting (A-67) into (A-66) gives the linear time-invariant model for the eliminator:

$$E(s) = \frac{(s+100)\,(s^2+200s+3.30\times10^5)\,(s^2+3.20\times10^5)^2}{(s+102)\,(s^2+126s+3.39\times10^5)\,(s^2+30.8s+3.26\times10^5)\,(s^2+41.8s+3.00\times10^5)} \qquad \text{(A-68)}$$

Bibliography

[1] Anderson, Brian D. O., and Moore, John B. *Optimal Control - Linear Quadratic Methods.* Englewood Cliffs, N.J.: Prentice-Hall, 1990.

[2] Athans, Michael. "The LQ-Servo with Integrators." *Lecture Notes on Multivariable Control,* Massachusetts Institute of Technology, 24 February 1986.

[3] Brogan, William L. *Modern Control Theory.* 3d. ed. Englewood Cliffs, N.J.: Prentice-Hall, 1991.

[4] Doerr, Christopher R. "Optical Reference Gyro Characterization and Performance Enhancement." Master of Science Thesis, Massachusetts Institute of Technology, 1990.

[5] Feldgoise, Stephan F. "Pointing Acquisition and Stabilization Test Bed." Master of Science Thesis, Massachusetts Institute of Technology, 1993.